SURFACE REFLECTANCE

(formerly ATMOSPHERIC CORRECTION OVER LAND)

VISIBLE/INFRARED IMAGER/RADIOMETER SUITE
ALGORITHM THEORETICAL BASIS DOCUMENT
Version 3: May 2000

Wenge Ni
Shawn W. Miller

Eric Vermote, Science Team Member
University of Maryland

RAYTHEON ITSS
4400 Forbes Boulevard
Lanham, MD 20706

SBRS Document #: Y2411

EDR: SURFACE REFLECTANCE

Doc No: Y2411

Version: 3

Revision: 0

	Function	Name	Signature	Date
Prepared by	EDR Developer	W. NI		
Approved by	Relevant IPT Lead	S. MILLER		
Approved by	Chief Scientist	P. ARDANUY		
Released by	Program Manager	H. BLOOM		

TABLE OF CONTENTS

LIST OF FIGURES

Raytheon

LIST OF TABLES

Raytheon

GLOSSARY OF ACRONYMS

ATBD	Algorithm Theoretical Basis Document
6S	Second Simulation of the Satellite Signal in the Solar Spectrum
AOT	Aerosol Optical Thickness
AVHRR	Advanced Very High Resolution Radiometer
BRDF	Bidirectional Reflectance Distribution Function
CrIS	Cross-track Infrared Sounder
DEM	Digital Elevation Model
DoD	Department of Defense
EDR	Environmental Data Record
EOS	Earth Observing System
GIFOV	Ground Instantaneous Field of View
IP	Intermediate Product
IPO	Integrated Program Office
LLLS	Low-level Light Sensor
MODIS	Moderate Resolution Imaging Spectroradiometer
MODTRAN	Moderate Resolution Atmospheric Radiance and Transmittance Model
NCEP	National Center for Environmental Prediction
NDVI	Normalized Distribution of Vegetation Index
NPOESS	National Polar-orbiting Operational Environmental Satellite System
OLS	Optical Line Scanner
OMPS	Ozone Mapping Profiling Suite
RT	Radiative Transfer
SDR	Sensor Data Record
SOS	Successive Order of Scattering
SZA	Solar Zenith Angle
TM	Thematic Mapper
TOA	Top of Atmosphere
VIIRS	Visible/Infrared Imager Radiometer Suite
VZA	Vertical Zenith Angle

ABSTRACT

The algorithm described in this document provides a correction of top of atmosphere (TOA) radiances for the Visible/Infrared Imager/Radiometer Suite (VIIRS) sensor by removing atmospheric effects to retrieve surface reflectance in ten VIIRS bands. These bands are centered at 0.412 µm, 0.445 µm, 0.488 µm, 0.555 µm, 0.645 µm, 0.865 µm, 1.24 µm, 1.61 µm (two different resolutions), and 2.25 µm. The algorithm corrects for the effects of gaseous, molecular, and aerosol scattering and absorption, as well as the coupling of the atmosphere and the surface bidirectional reflectance, using a lookup table (LUT) based upon a radiative transfer model (6S). The correction uses aerosol information from VIIRS aerosol Environmental Data Records (EDRs), complemented by water vapor from VIIRS, National Center for Environmental Prediction (NCEP) feeds, or the Conical-scanning Microwave Imager/Sounder (CMIS); surface pressure from NCEP; and column ozone from the Ozone Mapping Profiling Suite (OMPS). The correction also uses a surface Bidirectional Reflectance Distribution Function (BRDF)/albedo model for coupling the atmosphere and surface anisotropic effect. It is applied to noncloudy pixels only.

This document presents the theoretical basis of the surface reflectance algorithm, adopted from the Moderate Resolution Imaging Spectroradiometer (MODIS) algorithm theoretical basis (Vermote, 1999). The quality of this product depends directly on the quality of the atmospheric correction algorithm, the accuracy of the atmospheric inputs, and the magnitude of the true surface reflectance. This document also addresses uncertainties due to errors in the algorithm, atmospheric inputs, and the surface BRDF effect. The sensitivity studies show that the major error source in the surface reflectance retrieval is that associated with the retrieval of aerosol optical thickness.

1.0   INTRODUCTION

1.1   PURPOSE

This Algorithm Theoretical Basis Document (ATBD) describes the algorithms used to retrieve the Surface Reflectance Intermediate Product (IP) from Visible/Infrared Imager/Radiometer Suite (VIIRS) measurements. It identifies the sources of input data, both VIIRS and non-VIIRS, that are required for surface reflectance retrievals. It provides the physical theory and mathematical background underlying their use in the retrievals, and it includes implementation details. The VIIRS Science Data System Team is using information continued in this document to establish the requirements and functionality of the data processing software.

1.2   SCOPE

This document covers the algorithm theoretical basis for the surface reflectances that will be routinely retrieved from VIIRS measurements. Other post-launch products are not discussed.

Section 1 of this ATBD describes the purpose and scope of the document. Section 2 provides an overview of the experiment. The processing concept and algorithm description are presented in Section 3. Section 4 summarizes assumptions and limitations, and references for publications cited in the text are provided in Section 5.

1.3   VIIRS DOCUMENTS

References to VIIRS documents will be indicated by numbers in italicized brackets, e.g., *[V-1]*.

 [V-1]   (40.3.1.1) Aerosol Optical Thickness

 [V-2]   (40.6.2) Normalized Difference Vegetation Index

 [V-3]   (40.6.4) Surface Type EDR

 [V-4]   Cloud Mask

1.4   REVISION

This is the third version of this document, dated May 2000. The second version of this document was dated June 1999. The first version was was dated October 6, 1998.

2.0   EXPERIMENT OVERVIEW

2.1   OBJECTIVES OF SURFACE REFLECTANCE RETRIEVALS

A number of VIIRS land products require surface reflectance as input. These include the top-of-canopy (TOC) Enhanced Vegetation Index (EVI) and Normalized Difference Vegetation Index (NDVI), Surface Type, and Snow Cover/Depth. The signal at the top of the atmosphere in a given VIIRS spectral band will contain information about both the surface and the atmosphere; the latter information must be removed to facilitate successful retrievals of the products listed above. Further, the products listed above feed into one another and into other VIIRS products, including Leaf Area Index (LAI), Active Fires, and Soil Moisture. It therefore becomes vital to derive an intermediate product (IP) for VIIRS that contains directional surface reflectances in all the relevant bands. In recognition of this, Raytheon adopted the MODIS surface reflectance algorithm as the baseline VIIRS approach. The latest version of the VIIRS SRD explicitly requires directional surface reflectances as part of the derivation of albedo, however the Surface Reflectance IP will remain a distinct product within the VIIRS processing architecture, and the ATBD will be kept separate. The V3 algorithm for Surface Albedo uses TOA reflectances instead of surface reflectances. TOA reflectances are described in the RDR-to-SDR ATBD.

The radiative transfer in the atmosphere and between the atmosphere and land surface can be expressed by a single RT model with specific lower boundary condition. However, solving this RT equation is complicated, requiring many approximations and a large number of calculations. Typically, analytical approximation methods in the atmospheric correction algorithm are used to decouple the scattering between land surface and atmosphere. The Second Simulation of the Satellite Signal in the Solar Spectrum (6S) developed at the Laboratoire d'Optique Atmospherique of Lille, France (Vermote *et al.,* 1995, 1997) is used in the Moderate Resolution Imaging Spectroradiometer (MODIS) atmospheric correction algorithm and other remote sensing applications.

Our plan for the VIIRS Surface Reflectance IP is to use the MODIS algorithm (Vermote, 1999) with 6S as a basis. Simulations presented in this document arose from the use of both 6S and MODTRAN; the model used for each particular sensitivity study will be detailed in the appropriate section of this document.

Operational implementation of this algorithm requires the use of a look-up table (LUT). The errors associated with using an LUT will be discussed in Section 3.4.1.

2.2   INSTRUMENT CHARACTERISTICS

The VIIRS instrument will now be briefly described to clarify the context of the descriptions of the Surface Reflectance IP presented in this document. VIIRS can be pictured as a convergence of three existing sensors, two of which have seen extensive operational use at this writing.

The Operational Linescan System (OLS) is the operational visible/infrared scanner for the Department of Defense (DoD). Its unique strengths are controlled growth in spatial resolution through rotation of the ground instantaneous field of view (GIFOV) and the existence of a low-level light sensor (LLLS) capable of detecting visible radiation at night. OLS has primarily served as a data source for manual analysis of imagery. The Advanced Very High Resolution

Radiometer (AVHRR) is the operational visible/infrared sensor flown on the National Oceanic and Atmospheric Administration (NOAA) Television Infrared Observation Satellite (TIROS-N) series of satellites (Planet, 1988). Its unique strengths are low operational and production cost and the presence of five spectral channels that can be used in a wide number of combinations to produce operational and research products. In December 1999, the National Aeronautics and Space Administration (NASA) launched the Earth Observing System (EOS) morning satellite, *Terra*, which includes the Moderate Resolution Imaging Spectroradiometer (MODIS). This sensor possesses an unprecedented array of thirty-two spectral bands at resolutions ranging from 250 m to 1 km at nadir, allowing for unparalleled accuracy in a wide range of satellite-based environmental measurements.

VIIRS will reside on a platform of the National Polar-orbiting Operational Environmental Satellite System (NPOESS) series of satellites. It is intended to be the product of a convergence between DoD, NOAA and NASA in the form of a single visible/infrared sensor capable of satisfying the needs of all three communities, as well as the research community beyond. As such, VIIRS will require three key attributes: high spatial resolution with controlled growth off nadir, minimal production and operational cost, and a large number of spectral bands to satisfy the requirements for generating accurate operational and scientific products.

Figure 1 illustrates the design concept for VIIRS, designed and built by Raytheon Santa Barbara Remote Sensing (SBRS). At its heart is a rotating telescope scanning mechanism which minimizes the effects of solar impingement and scattered light. VIIRS is essentially a combination of SeaWiFS foreoptics and an all-reflective modification of MODIS/THEMIS aft-optics. Calibration is performed onboard using a solar diffuser for short wavelengths and a blackbody source and deep space view for thermal wavelengths. A solar diffuser stability monitor (SDSM) is also included to track the performance of the solar diffuser. The nominal altitude for NPOESS will be 833 km. The VIIRS scan will therefore extend to 56 degrees on either side of nadir.

The VIIRS SRD places explicit requirements on spatial resolution for the Imagery EDR. Specifically, the horizontal spatial resolution (HSR) of bands used to meet threshold Imagery EDR requirements must be no greater than 400 m at nadir and 800 m at the edge of the scan. This led to the development of a unique scanning approach which optimizes both spatial resolution and signal to noise ratio (SNR) across the scan. The concept is summarized in Figure 2 for the imagery bands; the nested lower resolution radiometric bands follow the same paradigm at exactly twice the size. The VIIRS detectors are rectangular, with the smaller dimension along the scan. At nadir, three detector footprints are aggregated to form a single VIIRS "pixel." Moving along the scan away from nadir, the detector footprints become larger both along track and along scan, due to geometric effects and the curvature of the Earth. The effects are much larger along scan. At around 32 degrees in scan angle, the aggregation scheme is changed from 3x1 to 2x1. A similar switch from 2x1 to 1x1 aggregation occurs at 48 degrees. The VIIRS scan consequently exhibits a pixel growth factor of only 2 both along track and along scan, compared with a growth factor of 6 along scan which would be realized without the use of the aggregation scheme. Figure 3 illustrates the benefits of the aggregation scheme for spatial resolution.

Passive Radiative Cooler (ETM+/MODIS/VIRS/IR&D)

Solar Calibration Port, Door and Screen
(ETM+/MODIS/SeaWiFS/VIRS)

Blackbody (MODIS/VIRS)

Aft Optics
(THEMIS)

Rotating Telescope Scan (SeaWiFS)

Electronics
Modules
(ETM+/MODIS,
SeaWiFS/VIRS)

Velocity

Nadir

- **Constant-Speed Rotating Telescope**
- **Simple All-Reflective Optics**
- **Proven Emissive/Reflective Calibration**
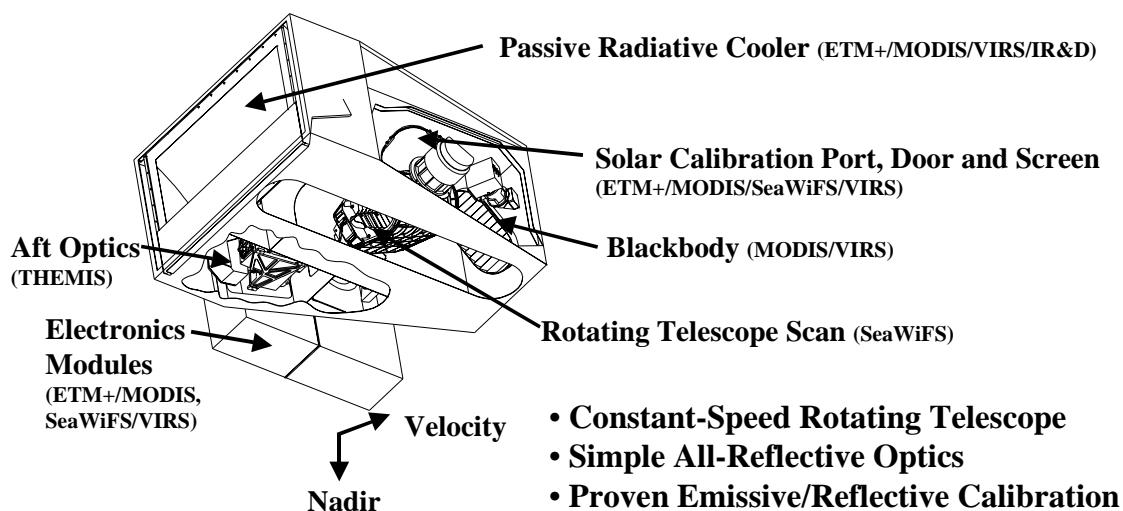
Figure 1. Summary of VIIRS design concepts and heritage.

Fine-Resolution Bands

Nadir

- aggregate 3 samples
- SNR increases by sqrt(3)

371 m

131 m

393 m

1700 km

- aggregate 2 samples
- SNR increases by sqrt(2)

547 m

309 m

617 m

3000 km

- no aggregation

800 m

800 m
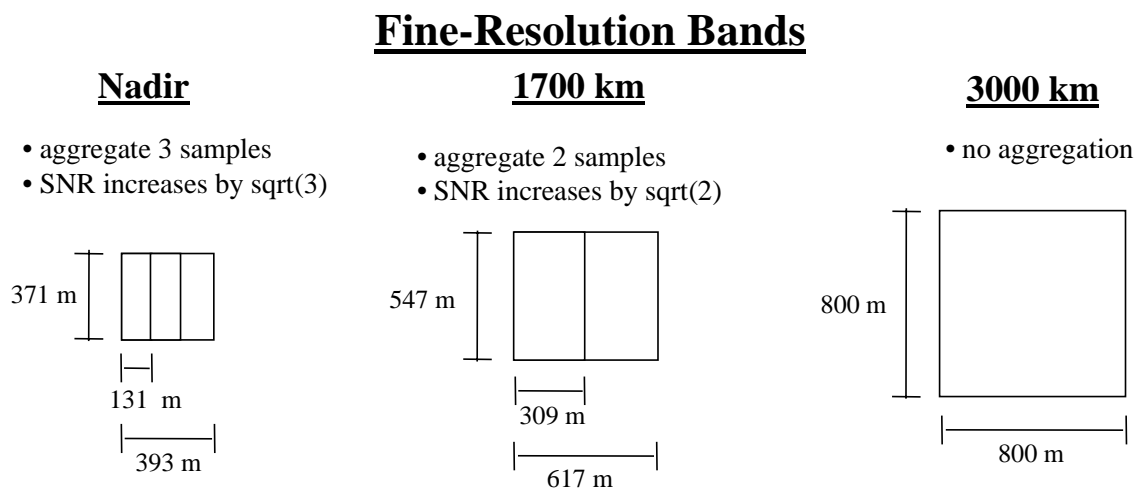
Figure 2. VIIRS detector footprint aggregation scheme for building "pixels."

Scan HSI as a Function of Scan Angle for Unit Raw GSD at Nadir
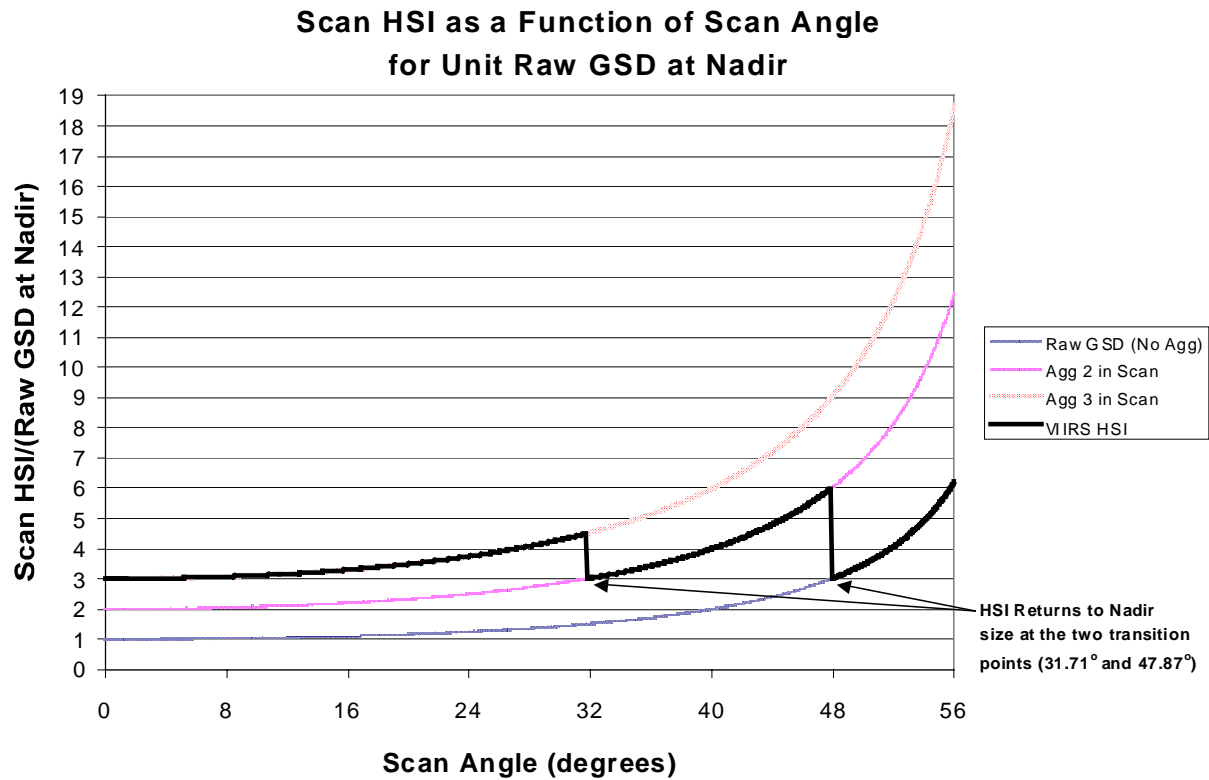
Figure 3. Benefits of VIIRS aggregation scheme in reducing pixel growth at edge of scan.

This scanning approach is extremely beneficial for the retrieval of land products such as the NDVI. The increasing importance of land cover change detection makes high spatial resolution in the NDVI or its input reflectances much more important, and SNR becomes a secondary issue (this latter point will be verified later in this document).

The VIIRS baseline performance is summarized in Table 1 and Table 2 for low and high radiances, respectively. The high radiance numbers are more relevant to land retrievals. The positioning of the VIIRS spectral bands is summarized in Figure 4 through Figure 7.

Table 1. VIIRS baseline performance and specifications, low radiance range.

			Nadir		31.71°		43.60°		47.80°		55.84°		Gain/	L/T typ Q/K	L/T max Q/K	3x1 Agg SNR @Ltyp	3x1 Agg NEDT @Ttyp	2x1 Agg SNR @Ltyp	2x1 Agg NEDT @Ttyp	Native SNR @Ltyp	Native NEDT @Ttyp	Native Spec SNR @Ltyp	Native Spec NEDT @Ttyp	SNR Margin (%)
Band	Wave (µm)	BW (µm)	Trk	Scn	Trk	Scn	Trk	Scn	Trk	Scn	Trk	Scn	TDI											
DNB	0.700	0.4000	742	742	742	742	742	742	742	742	742	742	variable	6.7E-05	500	n/a	n/a	n/a	n/a	8.0	n/a	6.0	n/a	33.3%
ch2w2	0.412	0.0200	742	262	895	393	1094	617	1213	786	1600	1600	D/1	44.9	135	752.3	n/a	614.2	n/a	434.3	n/a	352.0	n/a	23.4%
2	0.445	0.0180	742	262	895	393	1094	617	1213	786	1600	1600	D/1	40.0	127	905.0	n/a	755.3	n/a	534.1	n/a	337.8	n/a	58.1%
ch8	0.488	0.0200	742	262	895	393	1094	617	1213	786	1600	1600	D/1	32.0	107	987.1	n/a	808.0	n/a	569.9	n/a	310.6	n/a	83.5%
4	0.555	0.0200	742	262	895	393	1094	617	1213	786	1600	1600	D/1	21.0	78	846.2	n/a	690.9	n/a	488.6	n/a	257.1	n/a	90.0%
5	0.645	0.0500	371	131	448	196	547	309	606	393	800	800	S/1	n/a	n/a	n/a	n/a	n/a	n/a	n/a	n/a	n/a	n/a	n/a
ec2	0.672	0.0200	742	262	895	393	1094	617	1213	786	1600	1600	D/1	10.0	69	584.7	n/a	477.4	n/a	337.6	n/a	242.1	n/a	39.4%
ec3	0.751	0.0150	742	262	895	393	1094	617	1213	786	1600	1600	S/1	9.6	41	481.1	n/a	392.8	n/a	277.8	n/a	199.1	n/a	39.5%
6	0.865	0.0390	371	131	448	196	547	309	606	393	800	800	S/1	n/a	n/a	n/a	n/a	n/a	n/a	n/a	n/a	n/a	n/a	n/a
6r	0.865	0.0390	742	262	895	393	1094	617	1213	786	1600	1600	D/1	6.4	29	823.4	n/a	672.3	n/a	475.4	n/a	215.3	n/a	120.8%
cd1	1.240	0.0200	742	262	895	393	1094	617	1213	786	1600	1600	S/1	n/a	n/a	n/a	n/a	n/a	n/a	n/a	n/a	n/a	n/a	n/a
7	1.378	0.0150	742	262	895	393	1094	617	1213	786	1600	1600	S/1	n/a	n/a	n/a	n/a	n/a	n/a	n/a	n/a	n/a	n/a	n/a
8	1.610	0.0600	371	131	448	196	547	309	606	393	800	800	S/1	n/a	n/a	n/a	n/a	n/a	n/a	n/a	n/a	n/a	n/a	n/a
8r	1.610	0.0600	742	262	895	393	1094	617	1213	786	1600	1600	S/1	0.42	16.3	54.0	n/a	44.1	n/a	31.2	n/a	14.6	n/a	113.5%
9	2.250	0.0500	742	262	895	393	1094	617	1213	786	1600	1600	S/1	0.12	5.6	24.1	n/a	19.7	n/a	13.9	n/a	10.8	n/a	30.3%
10w	3.740	0.3800	371	131	448	196	547	309	606	393	800	800	S/1	270	353	17.1	1.108	14.0	1.356	9.9	1.918	7.0	2.436	27.0%
10r	3.700	0.1800	742	262	895	393	1094	617	1213	786	1600	1600	S/1	270	310	131.7	0.142	107.5	0.174	76.0	0.247	47.3	0.396	60.6%
ext2	4.050	0.1550	742	262	895	393	1094	617	1213	786	1600	1600	D/1	300	338	823.6	0.031	672.6	0.038	475.5	0.053	237.7	0.107	100.0%
est4	8.550	0.3000	742	262	895	393	1094	617	1213	786	1600	1600	S/1	270	306	1616.1	0.027	1319.5	0.033	933.1	0.046	475.0	0.091	96.1%
11	10.7625	1.0000	742	262	895	393	1094	617	1213	786	1600	1600	S/1	260	310	1119.8	0.045	914.3	0.055	646.5	0.078	408.7	0.123	58.2%
12w	11.450	1.9000	371	131	448	196	547	309	606	393	800	800	S/1	210	310	82.1	0.426	67.1	0.522	47.4	0.738	23.3	1.500	103.2%
12r	12.0125	0.9600	742	262	895	393	1094	617	1213	786	1600	1600	S/2	270	310	1424.2	0.042	1162.8	0.052	822.2	0.073	448.8	0.134	83.2%

Table 2. VIIRS baseline performance and specifications, high radiance range.

			Nadir		31.71°		43.60°		47.80°		55.84°		Gain/	L/T typ Q/K	L/T max Q/K	3x1 Agg SNR @Ltyp	3x1 Agg NEDT @Ttyp	2x1 Agg SNR @Ltyp	2x1 Agg NEDT @Ttyp	Native SNR @Ltyp	Native NEDT @Ttyp	Native Spec SNR @Ltyp	Native Spec NEDT @Ttyp	SNR Margin (%)
Band	Wave (µm)	BW (µm)	Trk	Scn	Trk	Scn	Trk	Scn	Trk	Scn	Trk	Scn	TDI											
DNB	0.700	0.4000	742	742	742	742	742	742	742	742	742	742	variable	n/a	n/a	n/a	n/a	n/a	n/a	n/a	n/a	n/a	n/a	n/a
ch2w2	0.412	0.0200	742	262	895	393	1094	617	1213	786	1600	1600	D/1	65.0	465	867.0	n/a	707.9	n/a	500.5	n/a	316.3	n/a	58.2%
2	0.445	0.0180	742	262	895	393	1094	617	1213	786	1600	1600	D/1	55.5	469	1152.3	n/a	940.9	n/a	665.3	n/a	409.8	n/a	62.4%
ch8	0.488	0.0200	742	262	895	393	1094	617	1213	786	1600	1600	D/1	51.8	541	1357.4	n/a	1108.3	n/a	783.7	n/a	414.3	n/a	89.1%
4	0.555	0.0200	742	262	895	393	1094	617	1213	786	1600	1600	D/1	29.0	590	1056.5	n/a	862.6	n/a	610.0	n/a	315.4	n/a	93.4%
5	0.645	0.0500	371	131	448	196	547	309	606	393	800	800	S/1	22.0	468	317.9	n/a	259.5	n/a	183.5	n/a	130.7	n/a	40.4%
ec2	0.672	0.0200	742	262	895	393	1094	617	1213	786	1600	1600	D/1	22.0	468	1031.6	n/a	842.3	n/a	595.6	n/a	406.0	n/a	46.7%
ec3	0.751	0.0150	742	262	895	393	1094	617	1213	786	1600	1600	S/1	n/a	n/a	n/a	n/a	n/a	n/a	n/a	n/a	n/a	n/a	n/a
6	0.865	0.0390	371	131	448	196	547	309	606	393	800	800	S/1	25.0	278	418.7	n/a	341.8	n/a	241.7	n/a	151.2	n/a	59.6%
6r	0.865	0.0390	742	262	895	393	1094	617	1213	786	1600	1600	D/1	25.0	278	1989.7	n/a	1624.6	n/a	1149	n/a	508.8	n/a	125.8%
cd1	1.240	0.0200	742	262	895	393	1094	617	1213	786	1600	1600	S/1	5.40	95	228.2	n/a	186.3	n/a	131.8	n/a	101.0	n/a	30.5%
7	1.378	0.0150	742	262	895	393	1094	617	1213	786	1600	1600	S/1	6.00	41	230.5	n/a	188.2	n/a	133.1	n/a	82.7	n/a	60.9%
8	1.610	0.0600	371	131	448	196	547	309	606	393	800	800	S/1	7.3	56.7	134.5	n/a	109.8	n/a	77.7	n/a	6.0	n/a	1194%
8r	1.610	0.0600	742	262	895	393	1094	617	1213	786	1600	1600	S/1	7.30	72.5	838.9	n/a	685.0	n/a	484.3	n/a	342.2	n/a	41.5%
9	2.250	0.0500	742	262	895	393	1094	617	1213	786	1600	1600	S/1	1.00	31.8	193.2	n/a	157.8	n/a	111.6	n/a	78.9	n/a	41.4%
10w	3.740	0.3800	371	131	448	196	547	309	606	393	800	800	S/1	n/a	n/a	n/a	n/a	n/a	n/a	n/a	n/a	n/a	n/a	n/a
10r	3.700	0.1800	742	262	895	393	1094	617	1213	786	1600	1600	S/1	300	353	512.0	0.045	418.0	0.055	295.6	0.078	165.3	0.140	78.8%
ext2	4.050	0.1550	742	262	895	393	1094	617	1213	786	1600	1600	D/1	335	500	2203.3	0.014	1799.0	0.018	1272	0.025	15.8	2.000	7954%
est4	8.550	0.3000	742	262	895	393	1094	617	1213	786	1600	1600	S/1	n/a	n/a	n/a	n/a	n/a	n/a	n/a	n/a	n/a	n/a	n/a
11	10.7625	1.0000	742	262	895	393	1094	617	1213	786	1600	1600	S/1	300	408	2235.7	0.030	1825.4	0.036	1291	0.052	950.6	0.070	35.8%
12w	11.450	1.9000	371	131	448	196	547	309	606	393	800	800	S/1	n/a	340	n/a	n/a	n/a	n/a	179.9	n/a	n/a	n/a	n/a
12r	12.0125	0.9600	742	262	895	393	1094	617	1213	786	1600	1600	S/2	300	340	2234.2	0.033	1824.2	0.040	1290	0.057	1024	0.072	25.9%
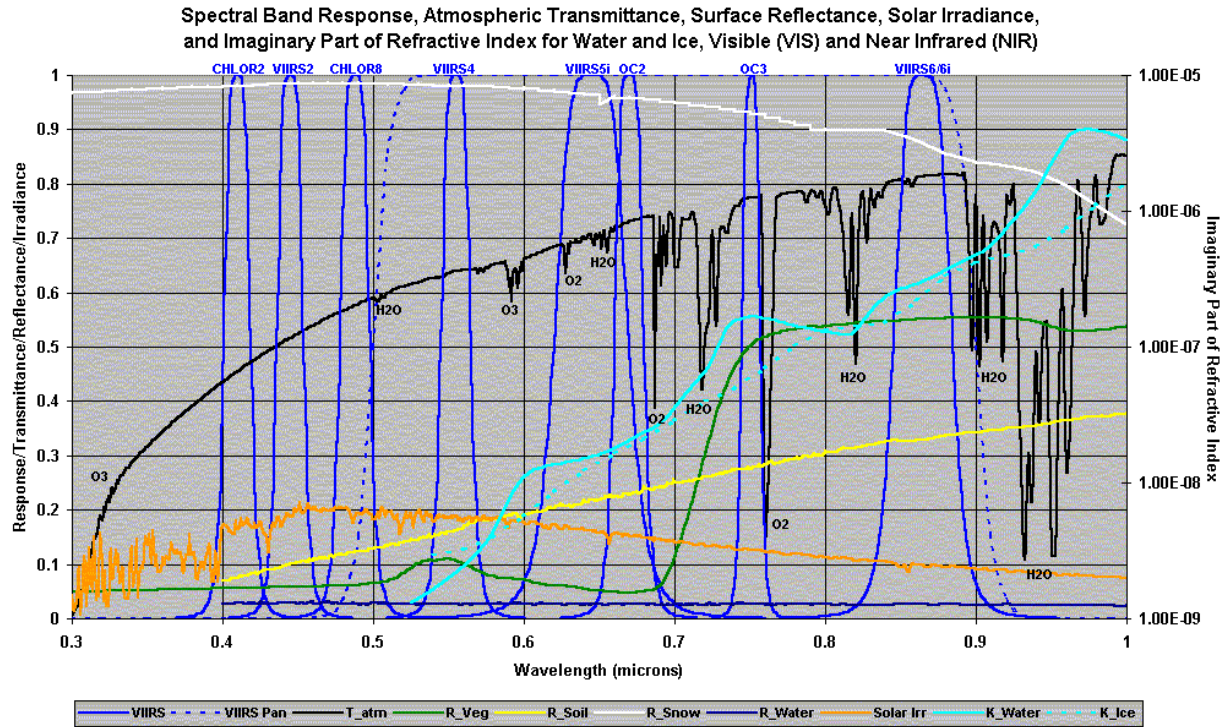
Figure 4. VIIRS spectral bands, visible and near infrared.
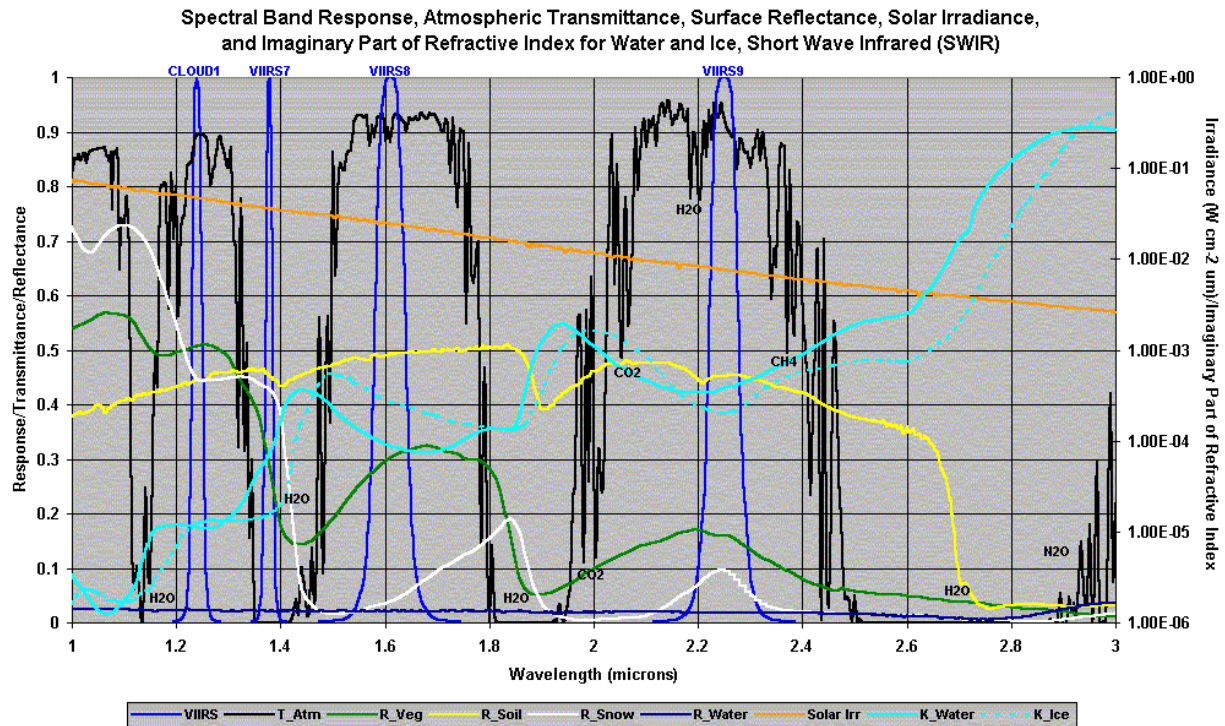
Figure 5. VIIRS spectral bands, short wave infrared.
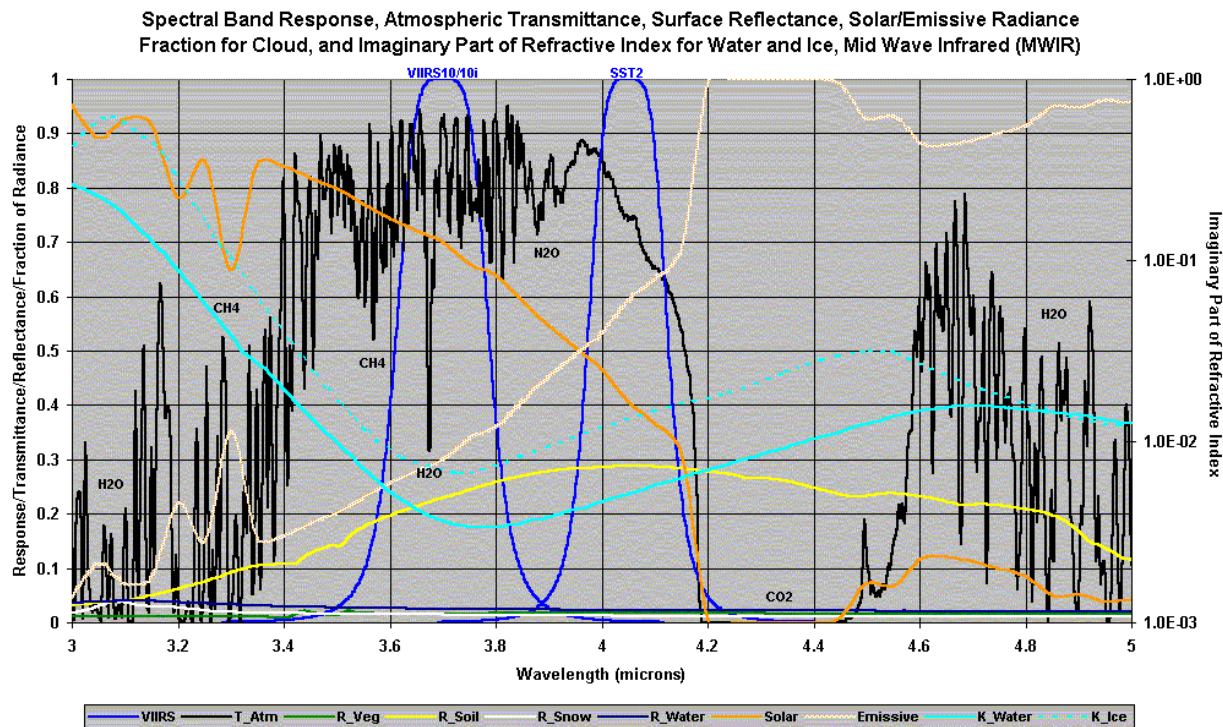
Figure 6. VIIRS spectral bands, medium wave infrared.
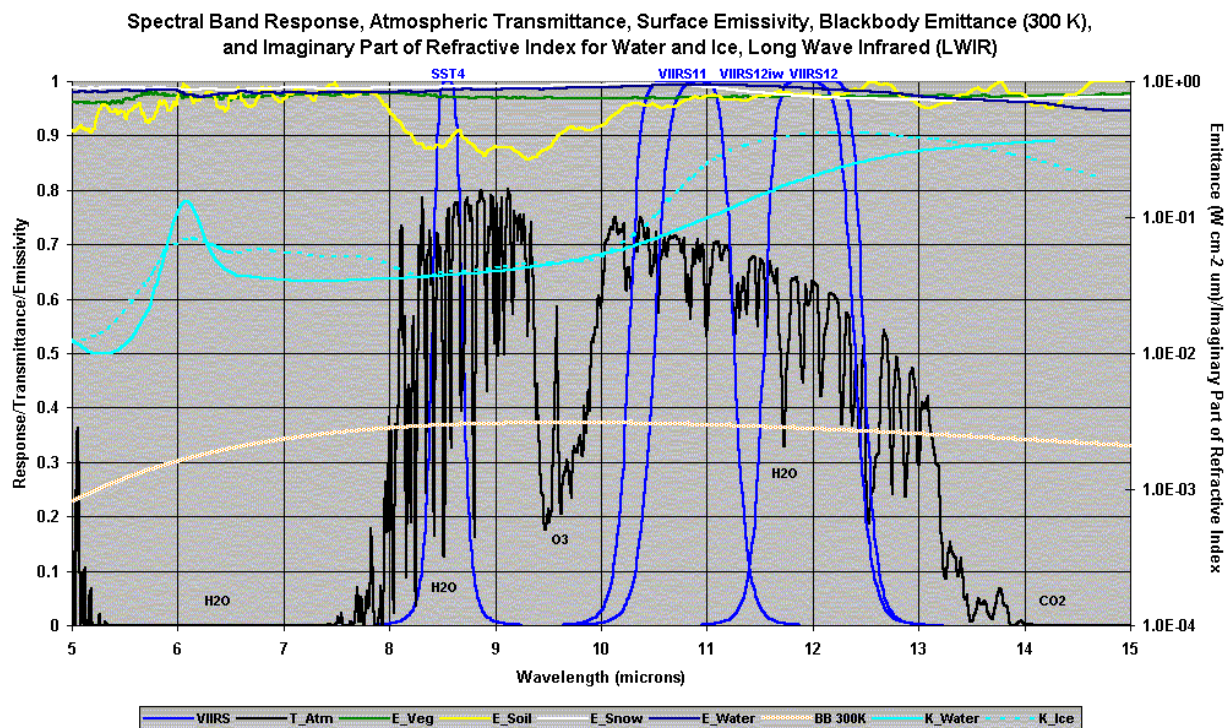
Figure 7. VIIRS spectral bands, long wave infrared.

2.3   RETRIEVAL STRATEGY

Retrievals of the Surface Reflectance IP will be conducted for all clear, land, daytime pixels within the array of NPOESS/VIIRS swaths. Daytime here is defined by a local solar zenith angle of 70 degrees or less, and clear is defined by a specification of "probably clear" or "definitely clear" by the VIIRS Cloud Mask IP. Land is defined by a land/sea mask, which is part of the Cloud Mask IP. "Land" in this sense is allowed to include inland water bodies.

Once a pixel has been categorized as clear, land, and daytime, the surface reflectance LUT will be implemented, using the VIIRS Calibrated Radiances SDR; the VIIRS Aerosol Optical Thickness EDR (including classification of aerosol type); the VIIRS Precipitable Water EDR; the VIIRS Surface Types—Biomes IP; and column ozone and surface pressure from NCEP analyses. Aerosol optical thickness and type, column water vapor, column ozone, TOA radiances, and solar/viewing geometry are inputs to the LUT. Surface pressure and elevation are required for a Rayleigh scattering correction, and biome type is required for the BRDF coupling correction.

The Surface Reflectance IP will be generated in nine VIIRS spectral bands, listed in Table 2.

Table 3. The nine VIIRS spectral bands in which Surface Reflectance will be computed.

Band Name	Center (microns)	Width (microns)
Chlor2	.412	.020
2	.445	.018
Chlor8	.488	.020
4	.555	.020
5i	.645	.050
6i	.865	.039
Cloud1	1.24	.020
8i	1.61	.060
9	2.25	.050

Raytheon

3.0   ALGORITHM DESCRIPTION

3.1   PROCESSING OUTLINE

Figure 1 shows the operational flowchart for the Surface Reflectance IP. After determination of clear/cloudy, land/ocean, and day/night for a given pixel, the heart of the process is the feeding of numerous inputs into a single LUT interpolation, resulting in directional surface reflectances in nine VIIRS bands.
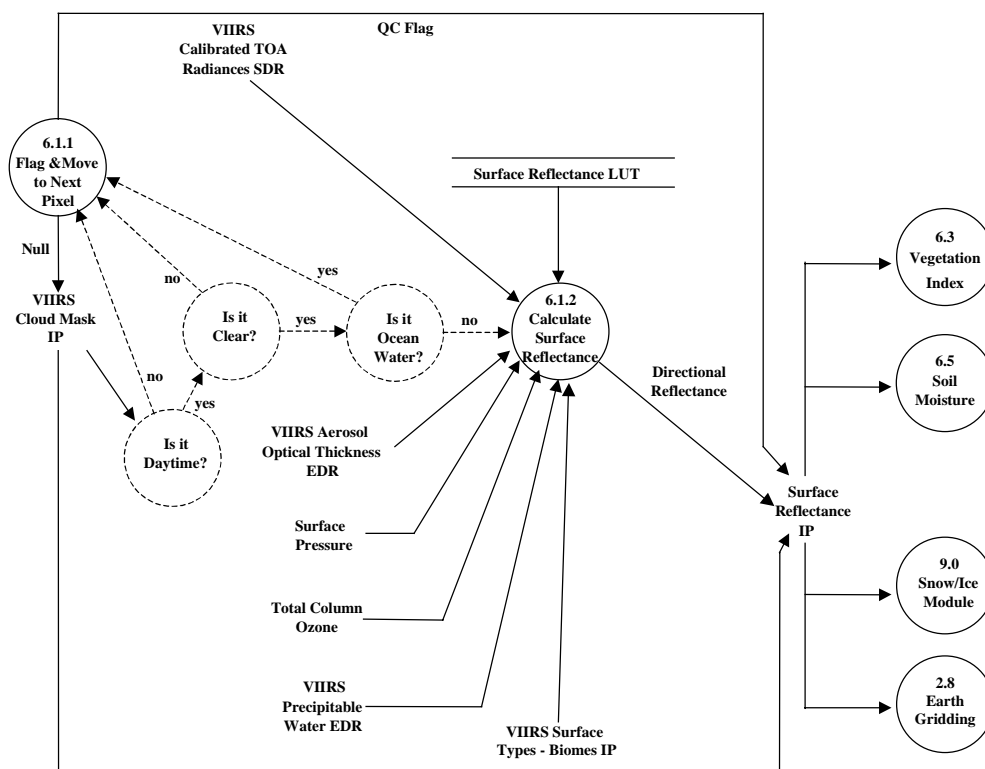
6.1 - SURFACE REFLECTANCE IP

Figure 8. Surface Reflectance IP processing architecture.

3.2   ALGORITHM INPUT

3.2.1   VIIRS Data

The Surface Reflectance IP algorithm employs the following VIIRS data:

- Aerosol Optical Thickness EDR (including aerosol type information)

- Precipitable Water EDR

- Calibrated TOA Radiances SDR (including radiances, geometry, geolocation, elevation)

- Cloud Mask IP (including cloud and land/water mask)

- Surface Types—Biomes IP

- Surface Reflectance LUT

3.2.2   Non-VIIRS Data

The Surface Reflectance IP algorithm employs the following non-VIIRS data:

- Surface Pressure from NCEP/NOGAPS analyses

- Column Ozone from Ozone Mapping Profiling Suite (OMPS)

3.3   THEORETICAL DESCRIPTION—PHYSICS AND MATHEMATICAL BACKGROUND

The atmospheric components affecting the remote sensing signal in the range of 0.4-2.5 μm are shown in Figure 9. Two atmospheric processes need to be removed from the atmospheric correction algorithm, in order to retrieve the solar radiance reflected by a target: absorption by gases (when observation bands are overlapping gaseous absorption bands); and scattering by aerosols and molecules. If the gaseous absorption is decoupled from scattering by assuming the absorbers are located above the scattering layers, the radiative transfer equation for a Lambertian homogeneous target of reflectance ρ_s at sea level altitude viewed by a satellite sensor with viewing zenith angle θ_v at certain illumination angle θ_s and relative azimuth angle between solar and viewing geometry ϕ is:

$$\rho_{TOA}(\mu_s, \mu_v, \phi) = T_g(\mu_s, \mu_v)\,[\rho_{R+A} + \frac{T_{R+A}(\mu_s)T_{R+A}(\mu_v)\rho_s}{1 - S_{R+A}\rho_s}] \tag{1}$$

where $\rho_{TOA}(\mu_s,\ \mu_v,\ \phi)$ is the reflectance at the top of the atmosphere; ρ_{R+A} is the intrinsic atmospheric reflectance (path reflectance), including the Rayleigh and aerosol scattering; $\rho_s(\mu_s,\mu_v,\phi)$ is the surface reflectance; $T_{R+A}(\mu_s)$ and $T_{R+A}(\mu_v)$ are the total upward and downward atmospheric transmission; S_{R+A} is the spherical albedo of the atmosphere; $\mu_s = cos(\theta_s)$ and $\mu_v = cos(\theta_v)$, where θ_s and θ_v are solar zenith and viewing zenith angles; and ϕ is the relative azimuth angle. T_g is the gaseous transmission for the solar radiation with H_2O, CO_2, O_2, and O_3 as

Raytheon

the principal absorbing gases. Other gases, such as CH_4, N_2O, and CO, are also taken into account in radiative transfer models such as 6S. The transmission is a nonlinear function of the effective amount of absorptive matter in the atmosphere, and depends also on the pressure and temperature profile. In the following, we will address the spectral properties of gas absorption, Rayleigh and aerosol scattering, and the coupling of the atmosphere scattering with the non-Lambertian surface. The 6S model bases its modeling of the atmospheric effects on:
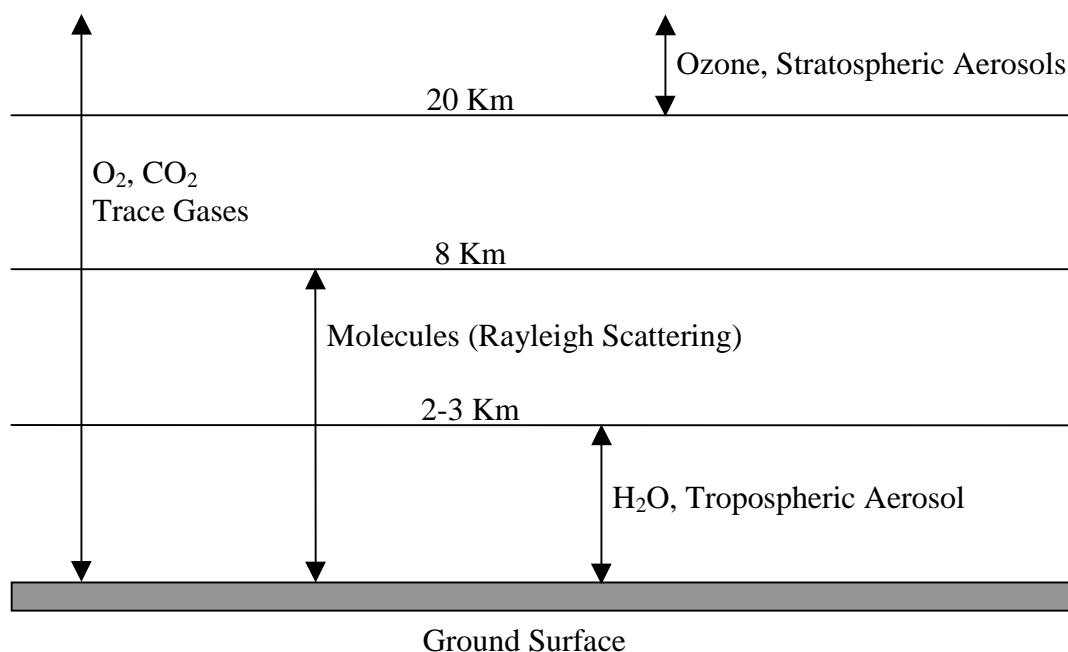
Figure 9. The atmospheric components affecting the remote sensing signal in the 0.4-2.5 μm range.

- An accurate approach of the absorption by atmospheric gases.

- A complete treatment of the scattering processes.

- An approximation of the interaction of the above two processes.

3.3.1 Gas Absorption

The most prominent gaseous absorbers in the atmosphere are water vapor (H_2O), carbon dioxide (CO_2), oxygen (O_2), ozone (O_3), methane (CH_4), nitrous oxide (N_2O), and carbon monoxide (CO). Gaseous absorption in the solar spectrum is displayed in Figure 10, which shows that: (1) H_2O exhibits absorption for wavelengths greater than 0.6 μm and gets stronger for wavelengths greater than 0.7 μm; (2) O_3 has absorption bands between 0.5-0.67 and is strongest around 0.58 μm; (3) CO_2 absorbs at 1.45 μm, 1.55-1.6 μm, 1.9-2.1 μm, and 2.65-2.85 μm; (4) O_2 absorbs quite strongly at 0.7 μm and 0.78 μm; (5) N_2O exhibits absorption around 2.85-2.95 μm; and (6) CH_4 absorbs at 2.2-2.4 μm.

Only the absorption by H_2O, O_3, and CO_2 occur significantly within VIIRS land bands. VIIRS band 8i (1.61 μm) has some CO_2 absorption; VIIRS bands 4 (0.555 μm) and 5i (0.645 μm) include O_3 and H_2O absorption; and band 6i (0.865 μm) contains a slight amount of H_2O absorption.

The incoming solar radiation is not strong at VIIRS band 8i, however it is an important band for discrimination of snow from clouds or other surface types. On the other hand, the absorption in this band is minimal, and CO2 is sufficiently well-mixed to effect negligible variability in TOA radiances at these wavelengths. We will therefore skip analysis of uncertainty of CO_2 input for the Surface Reflectance IP algorithm. The major absorption gases considered here are H_2O and O_3.

3.3.2   Rayleigh and Aerosol Scattering

Figure 11 shows the optical properties of different aerosols, including stratospheric aerosol, maritime aerosol, deserment aerosol, biomass aerosol, continental aerosol, and urban aerosol. The locations of nine sample remote sensing bands, both from VIIRS and from MODIS, are overlaid on the plots. As the figure shows, stratospheric, maritime, desertic, and continental aerosols have high single scattering albedo in the visible and mid-infrared portion of the spectrum, and urban aerosol has the lowest single scattering albedo. The six types of aerosols have similar asymmetry in visible and mid-infrared wavelengths, but quite different asymmetry when the wavelength is greater than 1.5 μm. All aerosol types have similar phase functions for scattering.

The molecular scattering properties, their phase functions, the spectral dependence of the optical thickness, and the depolarization factor are well known and stable. However, the aerosol scattering properties are variable (Vermote *et al.,* 1997). For a given aerosol model, the phase function and extinction and absorption coefficients have to be computed as a function of the wavelength. The optical properties of each spherical particle, as well as the size distribution of the particles, are the parameters used in the Mie scattering calculation. The scattering of aerosol and Rayleigh is approximated by successive order of scattering (SOS).
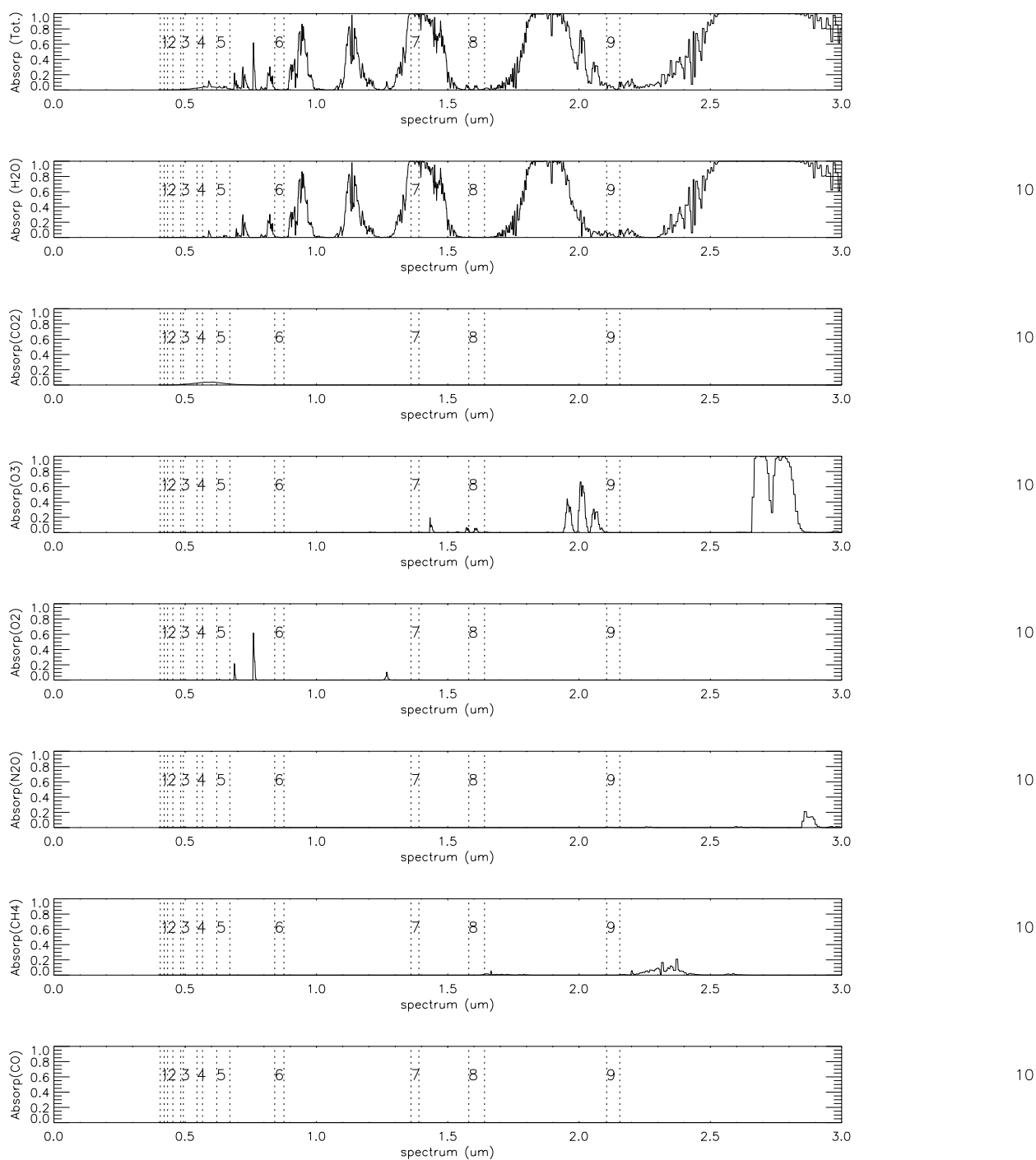
Figure 10. Atmospheric gaseous absorption spectrum. Several sample remote sensing bands overlaid for reference. Note: band "7" (1.38 μm) is purposely located in a water vapor absorption band for upper atmosphere utility.
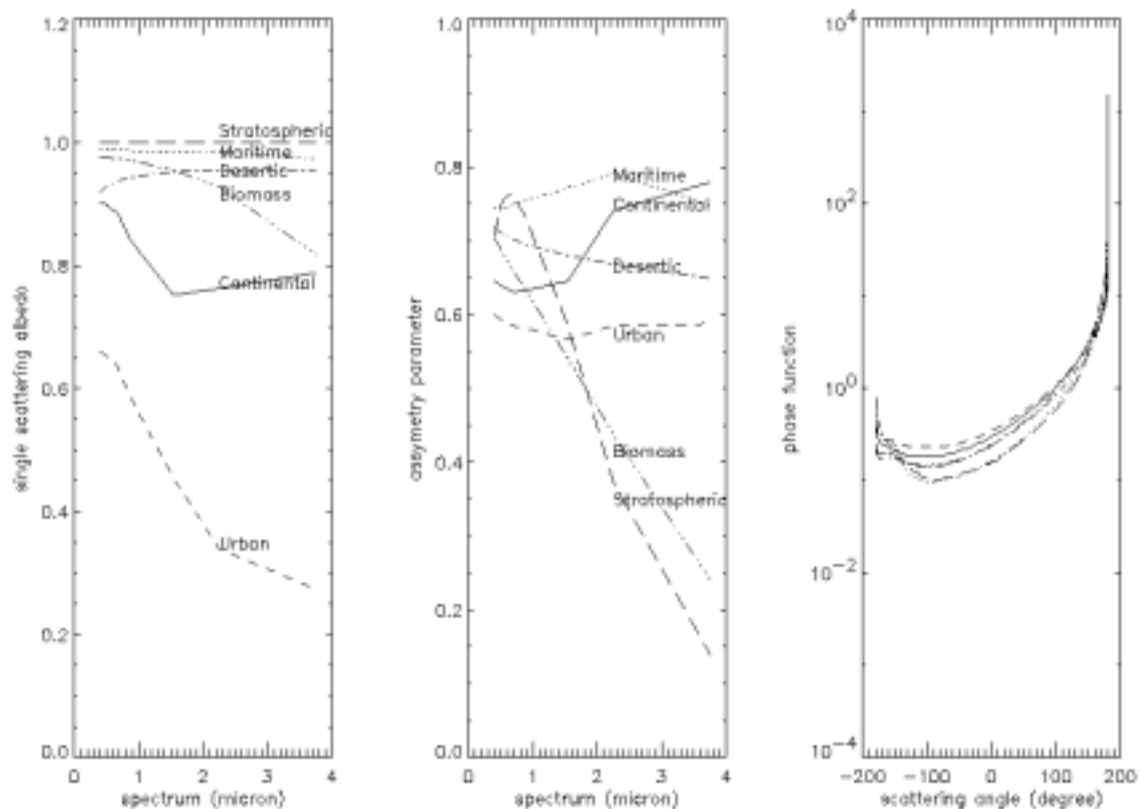
Figure 11. Scattering properties (single scattering albedo, asymmetry parameter, phase function) of different aerosol types.

Figure 12 shows the spectral properties of aerosol and molecular Rayleigh scattering, again with nine sample remote sensing bands overlaid. Both Rayleigh scattering and aerosol spherical albedo decrease with wavelength, with stronger decreases for Rayleigh scattering. For wavelengths less than 0.5 μm, Rayleigh scattering is greater than aerosol scattering; for wavelengths greater than 0.5 μm, aerosol scattering is greater than Rayleigh scattering. When the wavelength is greater than 0.75 μm, aerosol scattering contributes to the total spherical albedo. Both the optical depth of aerosols and molecular scattering decrease with wavelength, with a stronger decrease for molecular scattering than for aerosols. The single scattering albedo of atmospheric molecules is very high (close to 1), and the single scattering albedo of aerosols is less than that of Rayleigh scattering. At the altitude of the satellite, the radiance consists of the following three components:

- Intrinsic atmospheric radiance, after the removal of atmospheric gas absorption, scattered by the molecules and aerosols in the atmosphere, which is dependent upon the scattering properties of molecules and aerosols and their optical thicknesses.

- The contribution of the total (direct plus diffuse) solar radiation reflected by the surface and directly transmitted from the surface to the sensor, which is related to the surface spectral properties and the atmospheric conditions.

- The contribution of the environment from surrounding areas, which reflects the total (direct plus diffuse) downward flux, reaching the sensor by scattering; this amount of contribution depends on atmospheric conditions and the spectral properties of land surfaces.

The radiance at the ground level also consists of three components:

- The solar radiance directly transmitted through the atmosphere.

- The diffuse radiance, after gas absorption and scattering by the atmosphere, reaching the ground.

- The radiance scattered between the atmosphere and the ground.

Figure 13 shows TOA reflectance and transmittance and their components with the change of wavelength. It shows that for vegetated land surfaces and wavelengths less than 0.52 μm, atmospheric intrinsic scattering is the major contributor to TOA reflectances. For wavelengths between 0.52 and 0.67 μm, the contributions from atmospheric intrinsic scattering and surface reflectance are comparable. For wavelengths greater than 0.67 μm, the surface reflectance is the major contributor to TOA reflectance, and the contribution from environmental reflectance is greater than the contribution from atmospheric intrinsic reflectance.

The major contribution from direct transmittance increases with wavelength in the atmospheric windows. The contribution from atmospheric diffuse transmittance is less than that from direct transmittance and decreases with wavelength. The contribution from environmental transmittance is relatively smaller.
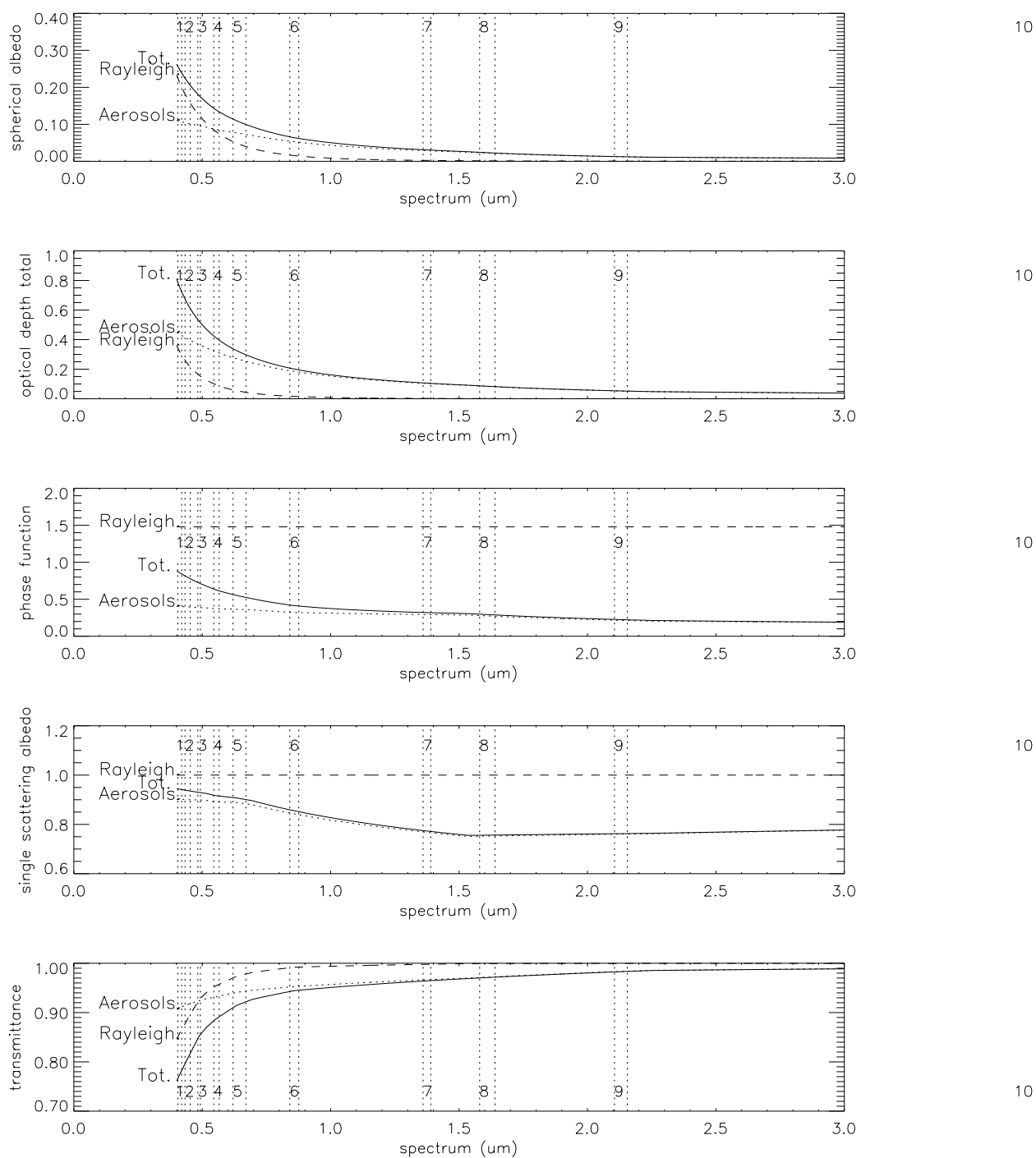
**Figure 12. The spectrum of Rayleigh and aerosol scattering.
Several sample remote sensing bands overlaid for reference.**
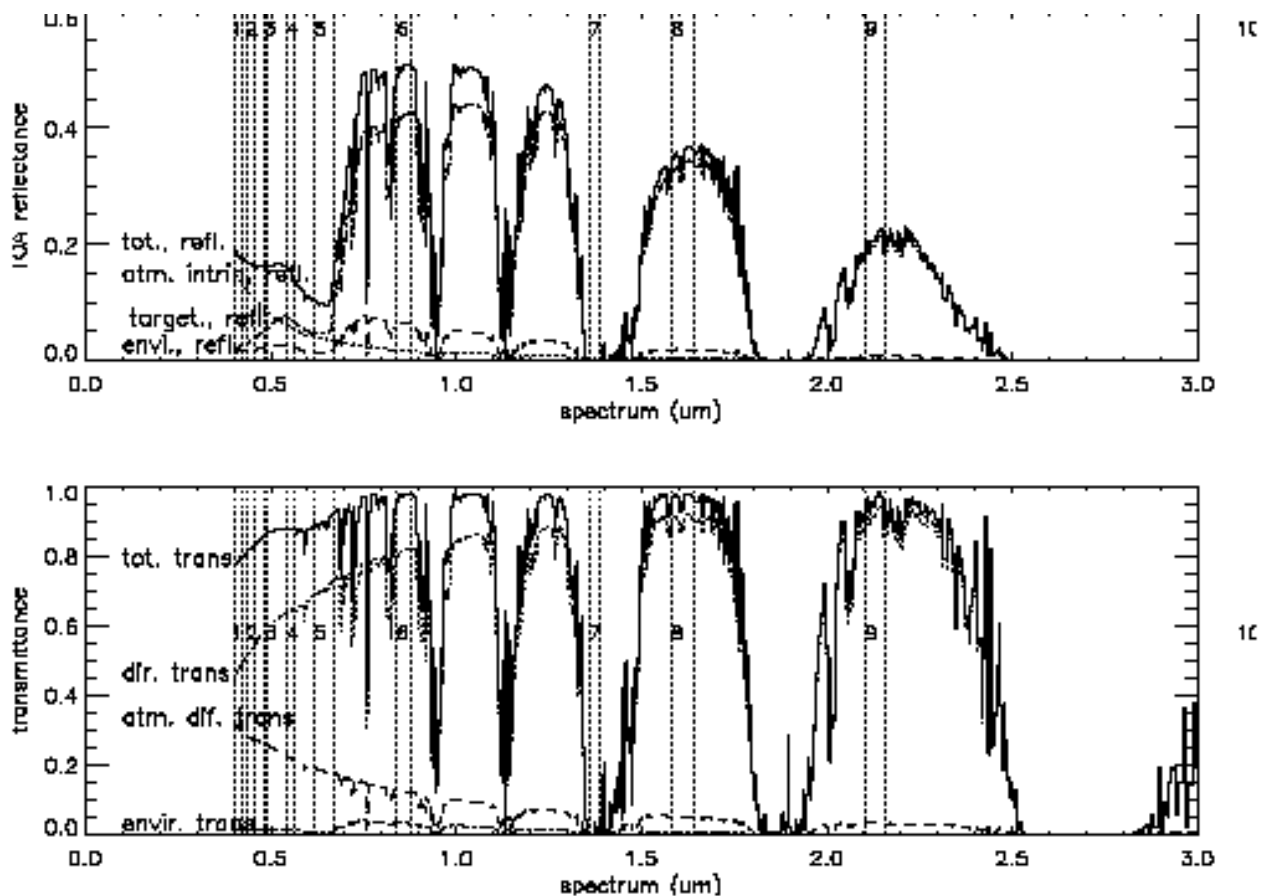
Figure 13. Simulated TOA reflectance and atmospheric transmittance over vegetated land surfaces using mid-latitude summer atmospheric conditions and the continental aerosol model. Several sample remote sensing bands are overlaid for reference.

3.3.3 Coupling of Scattering and Absorption

The transmission resulting from gaseous absorption is calculated exactly in 6S. The transmission and reflectances from molecules or aerosol scattering are computed by numerical methods. They are separated when both effects occur simultaneously. Although this separation is appropriate for ozone, it is not appropriate for water vapor.

The coupling between absorption by water vapor and scattering from aerosols can be important, as the aerosols and water vapor can be located at the same level in the atmosphere (2-3 km). 6S cannot handle the problem in a precise way, because the absorption should be computed along every path after each scattering event. Three cases are considered in 6S: (1) water vapor above the aerosol layer (maximum absorption i=3 in the following equation); (2) water vapor under the aerosol layer (minimum absorption i=1 in the following equation); and (3) an average case where half of the water vapor present in the atmosphere absorbs the aerosol path radiance (i=2 in the following equation). Equation 1 is modified in 6S as:

$$
\rho_{TOA}^{i=1,3}(\mu_s,\mu_v,\phi) = T_g^{OG}(\mu_s,\mu_v)[\rho_R + (\rho_{R+A} - \rho_R)T_g^{H_2O}(\theta_s,\theta_v,\frac{i-1}{2}U_{H_2O})
$$
$$
+ \frac{T_{R+A}(\mu_s)T_{R+A}(\mu_v)\rho_s}{1-S_{R+A}\rho_s}T_g^{H_2O}(\theta_s,\theta_v,U_{H_2O})] \tag{2}
$$

$T_g^{OG}(\mu_s,\mu_v)$ is the gaseous absorption for gases other than water vapor, $T_g^{H_2O}(\theta_s,\theta_v,\frac{i-1}{2}U_{H_2O})$ is the H$_2$O absorption, and $(\rho_{R+S} - \rho_R)$ is an estimate of the aerosol intrinsic reflectance.

3.3.4 Surface BRDF Effect

For a non-Lambertian surface, the coupling of the atmosphere and the land surface are rather complicated. The reflectance in the solar spectrum at the TOA is expressed in 6S as:

$$
\rho_{TOA}(\mu_s,\mu_v,\phi) = \rho_{R+A} + e^{-\frac{\tau}{\mu_v}}e^{-\frac{\tau}{\mu_s}}\rho_s(\mu_s,\mu_v,\phi) + e^{-\frac{\tau}{\mu_v}}t_d(\mu_s)\overline{\rho} + e^{-\frac{\tau}{\mu_s}}t_d(\mu_v)\overline{\rho'}
$$
$$
+ t_d(\mu_s)t_d(\mu_v)\overline{\overline{\rho}} + \frac{T_{R+A}(\mu_s)T_{R+A}(\mu_v)S_{R+A}(\overline{\overline{\rho}})^2}{1-S_{R+A}\overline{\overline{\rho}}} \tag{3}
$$

where $\overline{\rho},\overline{\rho'},\overline{\overline{\rho}}$ are the surface hemispherical-directional, directional-hemispherical, and hemispherical-hemispherical (spherical) reflectances (albedo), respectively. The latter terms, also called coupling terms, couple the atmospheric radiative transfer with the surface reflectance properties. They are defined as:

$$
\overline{\rho}(\mu_s,\mu_v,\phi) = \frac{\int_0^{2\phi}\int_0^1 \mu L_{R+A}^{\downarrow}(\tau_A,\tau_R,\mu_s,\mu_v,\phi')\rho_s(\mu_s,\mu_v\phi'-\phi)\,d\mu d\phi'}{\int_0^{2\phi}\int_0^1 \mu L_{R+A}^{\downarrow}(\tau_A,\tau_R,\mu_s,\mu_v,\phi')\,d\mu d\phi'} \tag{4}
$$

$$\overline{\rho}'(\mu_s, \mu_v, \phi) = \overline{\rho}(\mu_v, \mu_s, \phi) \tag{5}$$

$$\overline{\overline{\rho}} = \overline{\overline{\rho}'(\mu_s, \mu_v, \phi)} \approx \frac{\int_0^1 \int_0^{2\phi} \int_0^1 \rho_s(\mu_s, \mu_v', \phi) \mu\mu' d\mu' d\phi d\mu}{\int_0^1 \int_0^{2\phi} \int_0^1 \mu\mu'\mu\mu' d\mu' d\phi d\mu} \tag{6}$$

where τ_R, τ_A are the Rayleigh and aerosol optical depth and $L_{R+A}^{\downarrow}(\tau_A, \tau_R, \mu_s, \mu_v, \phi')$ is the downwelling diffuse irradiance with the sun at μ_s.

For given atmosphere optical parameters and estimates of the surface reflectance, the coupling terms from (5) and (6) can be calculated, allowing atmospherically corrected actual surface reflectances to be obtained from observed values of ρ_{TOA} by solving (3). Operationally, initial estimates of surface reflectances may be taken either from *a priori* knowledge of surface reflectance properties or from an independent surface reflectance data product. Surface reflectance may be computed from a surface BRDF model.

To give more weight to the actual observations than to the estimated surface BRDF used in the calculation of the coupling terms, Vermote *et al.* (1997) used the ratio between the estimated BRDF (ρ_s^m) coupled with the atmosphere and the actual surface BRDF (ρ_s) to correct the measured values:

$$
\begin{aligned}
\rho_{TOA}(\mu_s, \mu_v, \phi) = p_{R+A} &+ e^{-\frac{\tau}{\mu_v}} e^{-\frac{\tau}{\mu s}} \rho_s(\mu_s, \mu_v, \phi) + \rho_s(\mu_s, \mu_v, \phi)[e^{-\frac{\tau}{\mu_v}} t_d(\mu_s)\overline{\rho^*} \\
&+ e^{-\frac{\tau}{\mu_s}} t_d(\mu_v)\overline{\rho'^*} + t_d(\mu_s) t_d(\mu_v)\overline{\overline{\rho^*}} \\
&+ \frac{TR + A(\mu_s)TR + A(\mu v)SR + A(\overline{\overline{\rho^*}})^2}{1 - SR + A\overline{\overline{\rho}}}]
\end{aligned}
\tag{7}
$$

where

$$\overline{\rho^*}(\mu_s, \mu_v, \phi) = \frac{\overline{\rho^m}(\mu_s, \mu_v, \phi)}{\rho_s^m(\mu_s, \mu_v, \phi)} \tag{8}$$

$$\overline{\rho^*}(\mu_s, \mu_v, \phi) = \overline{\rho^*}(\mu_v, \mu_s, \phi) \tag{9}$$

$$\overline{\overline{\rho^*}}(\mu_s, \mu_v, \phi) = \frac{\overline{\overline{\rho^m}}(\mu_s, \mu_v, \phi)}{\rho_s^m(\mu_s, \mu_v, \phi)} \tag{10}$$

The surface reflectance ρ_s can be obtained by solving a (7). In the above approach, only the shape of the BRDF influences the correction process and not the actual magnitude of the

estimated BRDF. This approach gives more weight to the actual observation than to the estimated BRDF.

When the surface is Lambertian, $\overline{\rho^*} = \overline{\rho'^*} = \overline{\overline{\rho^*}} = 1$ and $\overline{\overline{\rho}} = \rho_s$, then (7) is simplified as:

$$\rho_{TOA}(\mu_s, \mu_v, \phi) = \rho_{R+A} + \frac{T_{R+A}(\mu_s)T_{R+A}(\mu_v)\rho_s}{1 - S_{R+A}\rho_s} \qquad (11)$$

In this case, ρ_s can easily be calculated without a prior estimate of the BRDF.

In our studies, we use both 6S and MODTRAN3.7 for forward modeling, simulating TOA radiances based on realistic VIIRS viewing geometry. A lookup table (LUT) generated from either 6S or MODTRAN3.7 is then used to perform the atmospheric correction in its inversion mode. We call atmospheric correction with the assumption of a Lambertian surface a "Lambertian-based atmospheric correction." Similarly, we call atmospheric correction with the assumption of a non-Lambertian surface a "BRDF-based atmospheric correction."

3.3.5 Surface Elevation Effects

For a target not at sea level, (1) is modified as:

$$\rho_{TOA}(\mu_s, \mu_v, \phi) = T_g(\mu_s, \mu_v, z_t)[\rho_{R+A}(z_t) + \frac{T_{R+A}(\mu_s, z_t)T_{R+A}(\mu_v, z_t)\rho_s}{1 - S_{R+A}(z_t)\rho_s}] \qquad (12)$$

The amount of scattering particles above the target (molecules and aerosols) and the amount of gaseous absorbents are related to the target altitude. Here the topographic data from a digital elevation model (DEM) is the input; it is used to calculate the atmospheric profile by stripping out the atmospheric level under target altitude.

The influences of target altitude on T_g are gas-dependent. Because the ozone layer is located in the upper levels of the atmosphere, the O_3 amount does not depend on target altitude, and transmission is not affected. On the other hand, as most water vapor is located in the lower atmosphere, water absorption is heavily affected by target altitude.

The effect of target altitude on molecular optical thickness, τ_r, is exactly accounted for. τ_r is linearly related to pressure at target level.

3.4 ALGORITHM SENSITIVITY STUDIES

The performance of the Surface Reflectance algorithm is limited by several key error sources, including the algorithm itself, sensor effects, atmospheric effects, and coupling of the atmosphere and surface BRDF. The atmospheric effects include aerosol and Rayleigh scattering, gaseous absorption, and thermodynamic conditions. The majority of the error for the VIIRS Surface Reflectance IP comes from uncertainties in the aerosol properties. The primary sensor effect is calibration error. Sensor noise is not a significant issue for most of the VIIRS bands with regard to surface reflectance retrievals.

Raytheon

The following error sources have been identified and will be detailed in the following subsections:

1) LUT Interpolation

2) Forward Modeling

3) Aerosol Optical Thickness

4) Aerosol Type

5) Column Ozone

6) Precipitable Water

7) Temperature Profile

8) Surface Pressure Retrieval/Rayleigh Scattering

9) BRDF Coupling

10) Cloud Mask

11) Sensor Noise

12) Sensor Calibration

Other errors exist, however most are negligible in comparison with a few key sources listed above, notably aerosols and calibration. Sensor modulation transfer function (MTF) errors can be significant over heterogeneous surfaces, however these are difficult to quantify on a global basis, and they will be deferred to the ATBDs for the downstream products such as the Vegetation Index EDR.

There are no explicit quality requirements on the Surface Reflectance IP in the VIIRS SRD. We have, however, derived performance estimates for surface reflectance retrievals to assist in the error budgeting for the VIIRS EDRs requiring this product as an input. Following the SRD, we have estimated performance in terms of three metrics: accuracy, precision, and uncertainty.

Consider a single true value T, the estimated values are X_i of T, where $i = 1, N$, the accuracy for T is

$$A = \left| \mu - T \right| \tag{13}$$

where $\mu = \frac{1}{N} \sum_{i=1}^{N} X_i$. The accuracy can be termed as a bias and is a direct comparison between the measurement X_i and the true value T.

For a single value of truth, the precision is defined as the standard deviation of the measurement:

$$P = \left[\frac{1}{N-1} \sum_{i=1}^{N} (X_i - \mu)^2 \right]^{\frac{1}{2}} \tag{14}$$

The calculation of the precision as defined is independent of the true value *T*.

The uncertainty U is defined as:

$$\text{U} \left[\frac{1}{N-1} \sum_{i=1}^{N} (X_i - T)^2 \right] \frac{1}{2} \tag{15}$$

The uncertainty is therefore akin to a root mean square (RMS) error between the estimated X_i and the true value T.

For variable truth data sets, the practical implementation of the definition on accuracy, precision, and uncertainty is to bin the possible values of T into small ranges which are large enough to provide a statistically significant number of test points.

The definitions of accuracy, precision and uncertainty in this case are:

$$\text{A} = \left[\mu - \mu T \right], \tag{16}$$

$$U = \left[\frac{1}{N-1} \sum_{i=1}^{N} (X_i - T_i)^2 \right]^{\frac{1}{2}} \tag{17}$$

$$\mathbf{P^1} = \left(\mathbf{U^2 - A^2} \right)^{1/2}, \tag{18}$$

where T_i is the true value corresponding to the measurements X_i,.

The results discussed in the following sections emerged from two main sets of simulations:

1) Scene simulations using Terrain Categorization (TERCAT) scenes based on Landsat TM imagery

2) "Stick modeling" simulations that deal with the radiative transfer for a single linear path through the atmosphere

In both cases, MODTRAN3.7 was the primary forward model used.

IPO-Supplied TERCAT Scenes

A limited degree of end to end testing was conducted using IPO-supplied TERCAT scenes. In particular, extracts from three scenes were investigated by the land team: Amazon, Olympic Peninsula, and Bangladesh. Results from the Amazon scene are deferred to the Vegetation Index ATBD. The other two scenes are shown in Figure 14 and Figure 15.
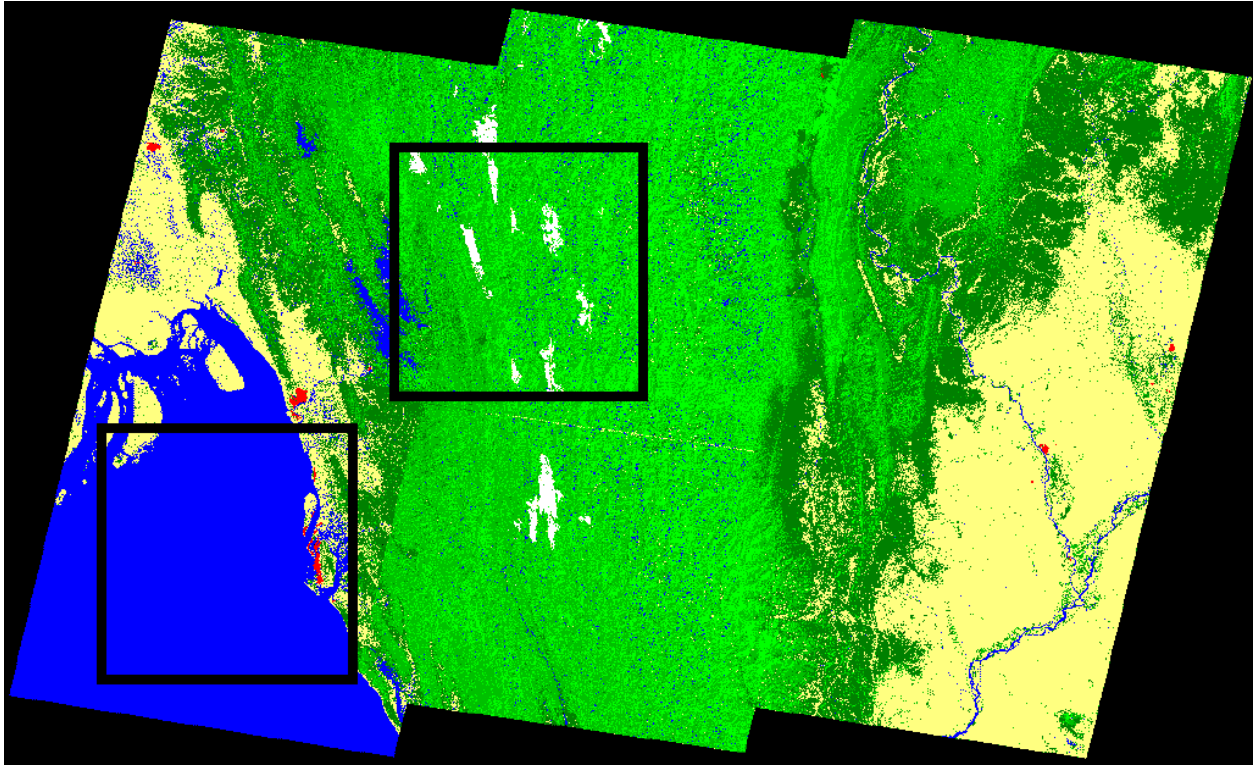
Figure 14. Classification map of the Bangladesh scene. Mostly forest (green), bare soil (sandy color), clouds (white), and water (blue). Boxes indicate subscenes for which sensitivity studies were conducted.
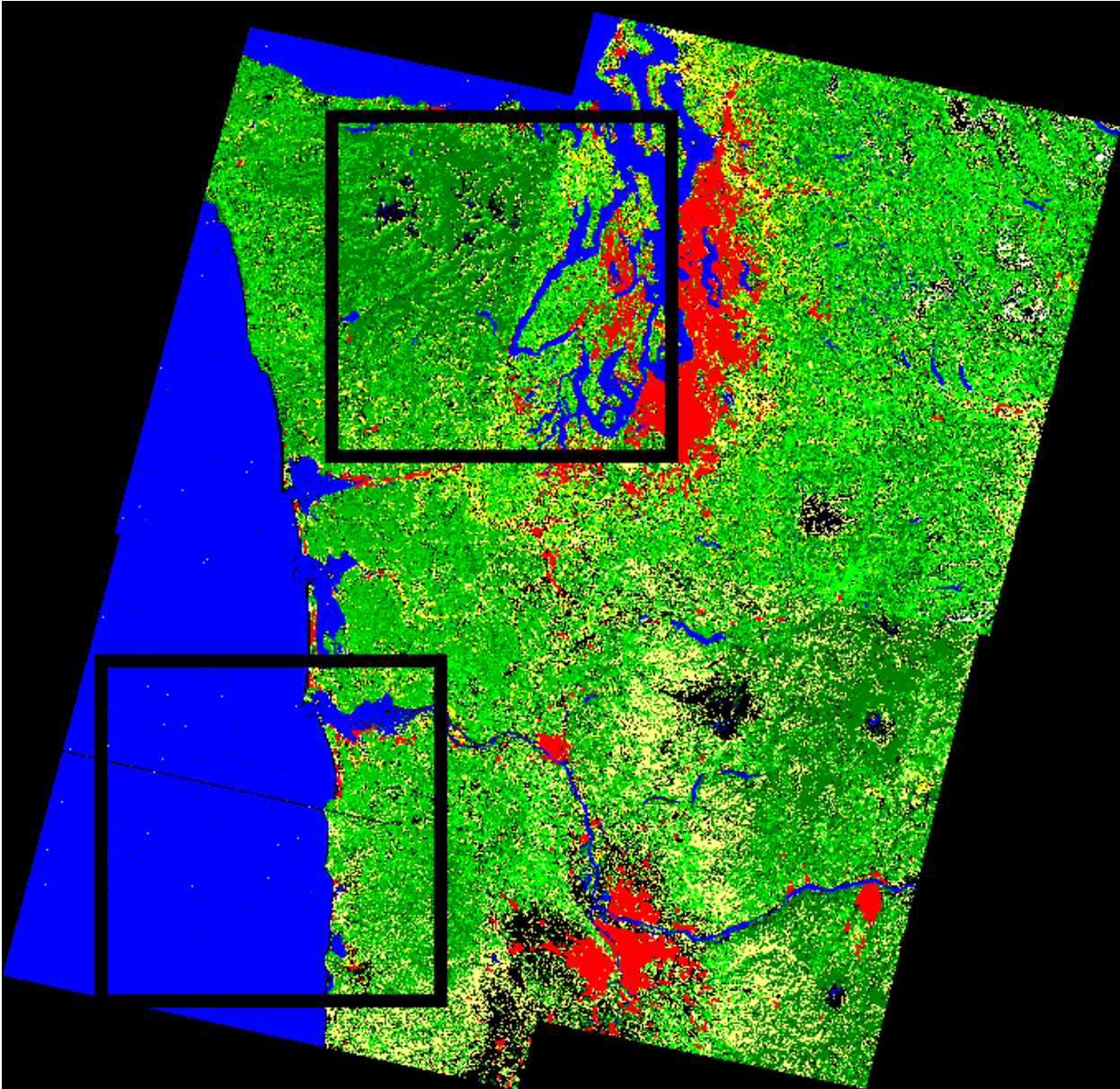
Figure 15. Classification map of the Olympic Peninsula scene. Very heterogeneous, with vegetation (green), water (blue), urban (red), and small amount of snow (white). Boxes indicate subscenes for which sensitivity studies were conducted.

Each TERCAT scene was handled in the following manner.

The TERCAT classification maps at 50-m resolution were converted to VIIRS surface spectral reflectances via the NPOESS spectral library, which includes data originating from the ASTER spectral library. These reflectances were used as inputs to forward modeling using MODTRAN 3.7. The surface reflectances and the independently supplied surface temperature map were aggregated to produce "truth" for surface reflectance, albedo, vegetation indices, and surface temperature. The dominant class in an aggregated VIIRS-sized pixel was chosen as truth for surface type.

Raytheon

For atmospheric effects, the MODTRAN midlatitude summer profile was used. Rural aerosols were applied, with aerosol optical thickness being spatially discretized into several image-wide bands ranging from approximately 0.2 to 0.8. Realistic viewing and solar geometry were applied using the SDP toolkit as though the data were obtained from a segment of a VIIRS swath.

The result of the forward modeling was a 50-m resolution map of top of atmosphere (TOA) radiances. These TOA radiances were spectrally integrated using a tophat response function with 100% transmittance, creating 16 VIIRS spectral bands for use by EDR algorithms. MTF blurring, sensor noise, and calibration errors were sequentially simulated as described in Hucks (1998). The output of this process was a simulated set of measured TOA radiances.

The retrieval pipeline started with cloud masking, followed by aerosol retrievals. Finally, various surface products were retrieved and compared with the truth. For Land EDRs and intermediate products (IPs), this included Surface Reflectance, Vegetation Index, Surface Albedo, and Surface Type.

Since the TERCAT scenes provided only a limited range of atmospheric and geometric conditions, the results of this processing were primarily used to confirm the MTF and BBR errors suggested from the Landsat TM simulations. The magnitude of the effects was similar between data sets for both error sources. MTF and BBR errors are discussed in detail in the Vegetation Index ATBD; they will not be considered in this document. Some results of aerosol, gaseous absorption, and temperature/pressure sensitivities presented here were derived from the TERCAT scene simulations.

Stick Modeling

The majority of the performance stratification work presented in the VIIRS Verification and Validation Plan is based upon a large ensemble of stick model simulations; the dimensions of this data set are summarized in Table 4.

Table 4. Summary of dimensions for Land EDR "stick modeling" data set.

Parameter	# Different Values	Range
Surface Type	10	Coniferous forest, deciduous forest, shrub, grass, crops, urban, snow, bare soil, desert sand, water
Solar Zenith	8	0-70 degrees
Scan Angle	7	0-60 degrees
Relative Azimuth	5	0-180 degrees
Aerosol Type	4	Urban, rural, desert, LOWTRAN maritime
Aerosol Optical Thickness	5	0.1-0.5

All forward modeling was conducted using MODTRAN 3.7, with a midlatitude summer profile. It was not deemed necessary to vary the profile, as water vapor, temperature, and ozone effects

are much smaller than the effects of aerosols in the VIIRS bands used for reflectance-based land EDRs.

The output of each stick model simulation consisted of a true broadband surface albedo, true TOA reflectances in nine spectral bands, and true surface reflectances in nine spectral bands. The bands are summarized in Table 3. The true reflectances were used to generated true values of NDVI and EVI at both top of canopy (TOC) and top of atmosphere (TOA).

3.4.1 LUT Interpolation

Since the Surface Reflectance algorithm is a finite LUT, calculations of surface reflectance will incur errors from interpolation between LUT elements. Figure 16 shows the effects for several VIIRS bands, based on simulations with the Olympic Peninsula TERCAT scene. In general, the errors are very small. Where the errors become larger, the solution is straightforward; the LUT can be given finer resolution to make all interpolation errors negligible.
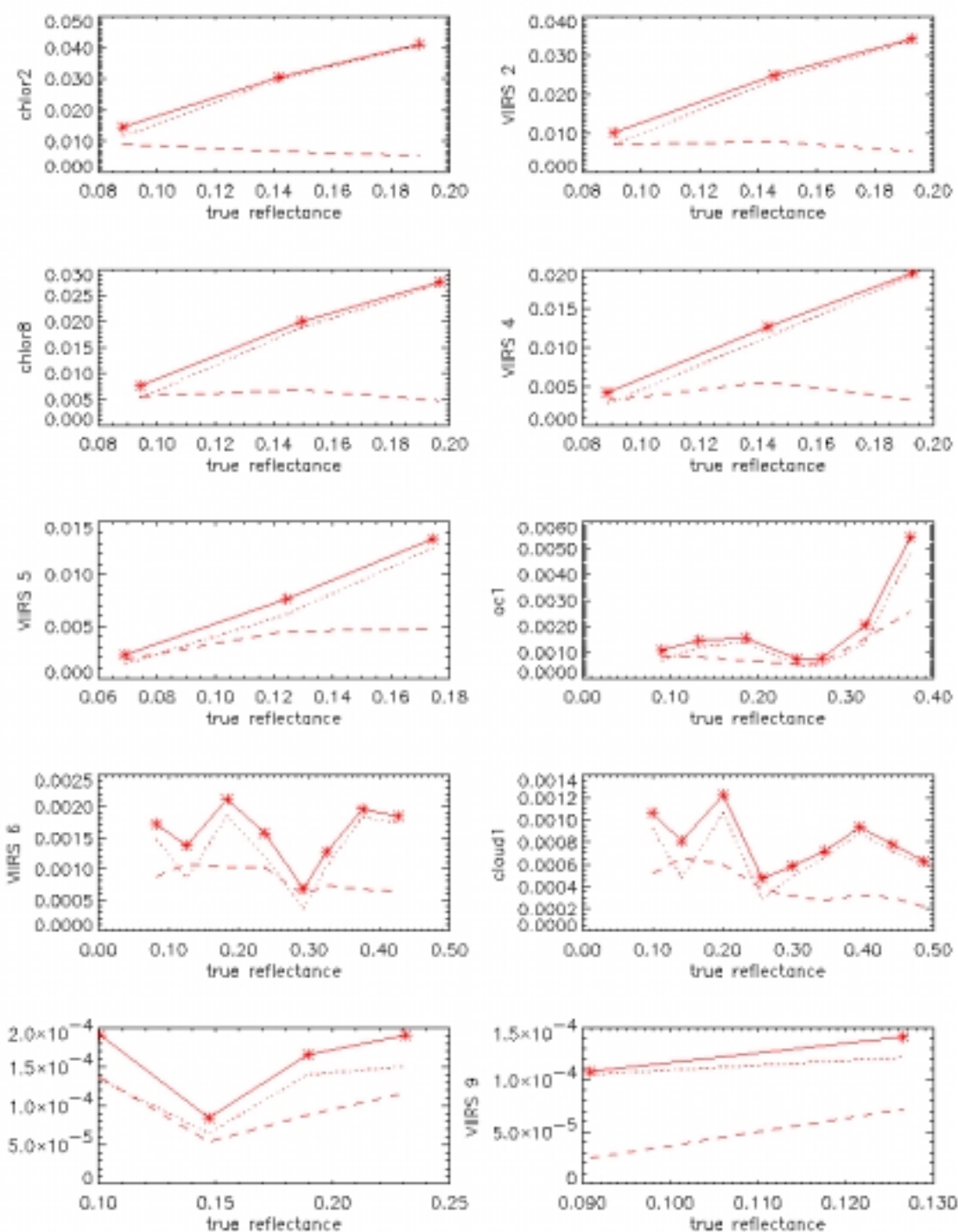
Figure 16. Interpolation error as a function of reflectance for several VIIRS bands, based on simulations with the Olympic TERCAT scene.

3.4.2 Forward Modeling

Any forward radiative transfer model will be an approximation to reality. Since the generation of a complete LUT for surface reflectance retrievals requires the use of a forward model in order to properly fill the necessary dimensions, a LUT-based surface reflectance algorithm will incur errors from the discrepancies between the model and a real atmosphere. For reflectance-based EDRs using window channels as on VIIRS, forward modeling error is primarily a measure of how well the model mimics the behaviors of aerosols. A global value of 3% in TOA radiance is allocated in the error budget, based upon the MODTRAN documentation (Kneizys et al, 1996).

As another means of investigating the effects of forward model error, we ran MODTRAN 3.7 in various atmospheric conditions, solar and viewing geometries to calculate the TOA radiance using a mid-latitude summer atmospheric model and a continental aerosol model. 6S was then used to retrieve surface reflectance under the same atmospheric conditions. Retrieved errors of surface reflectances over different land surfaces using MODTRAN 3.7 in the forward simulation and 6S in the retrieval are shown in Figure 17. The indices for the surface types in Figure 17 are listed in Table 5 below. The results presented here suggest that errors in the retrieved surface reflectance using different forward and backward models range from 0.0 to 0.033 over different land surface types. The largest errors are in the shortest wavelength VIIRS bands. The smallest are in VIIRS bands 5 and 6, with a relatively larger error for mixed shrub/scrub land surface, which is relatively dark.   These numbers lend credence to the initial error budget allocation.

Table 5. Surface types considered for the results of the forward model error simulations.

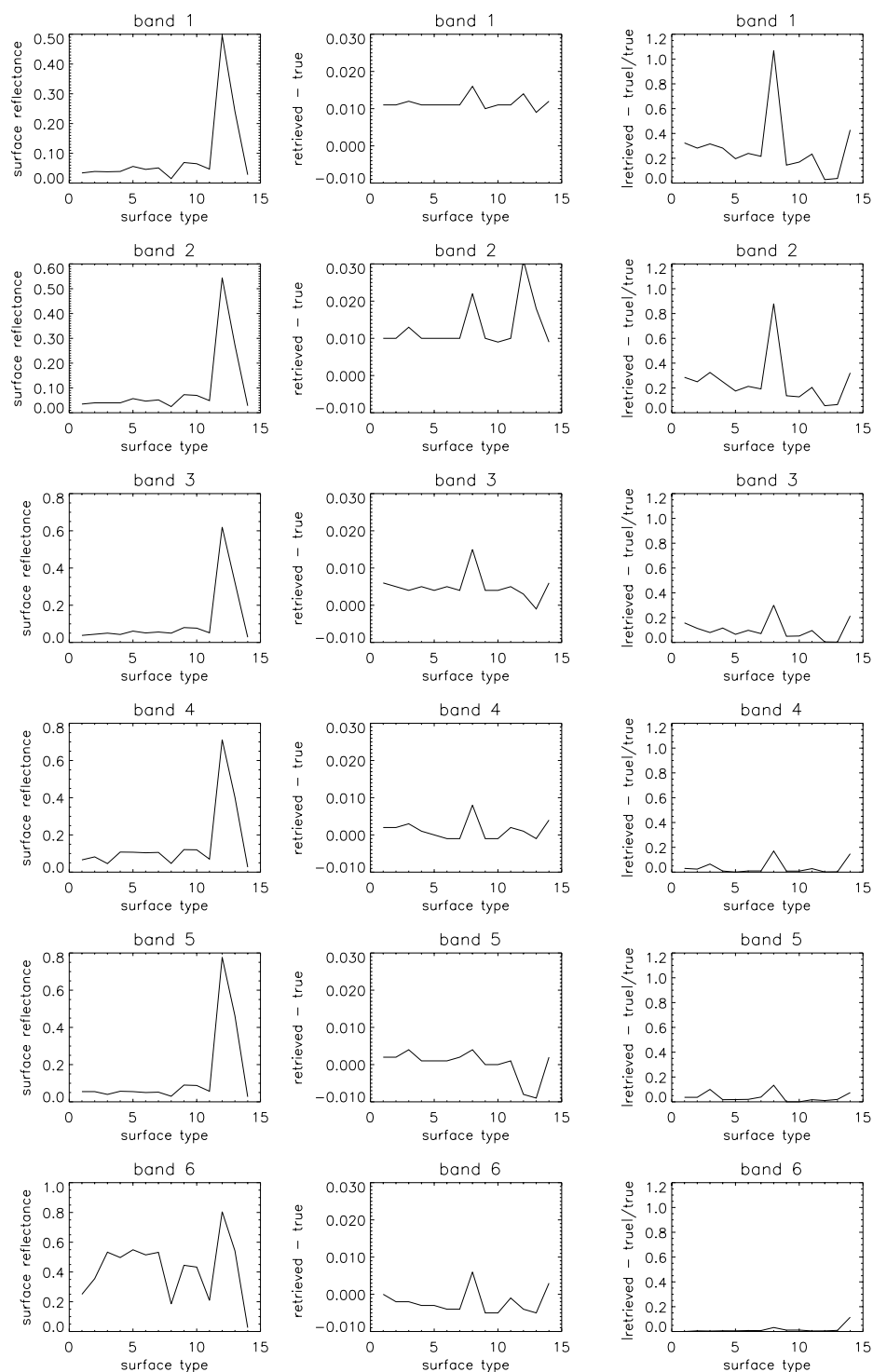| Number	Surface Type
1	Developed-High Intensity
2	Developed-Low Intensity
3	Cropland
4	Grassland
5	Deciduous Forest
6	Evergreen Forest
7	Mixed Forest
8	Mixed Shrub/Scrub
9	Palustrine Forest
10	Estuarine Emergent Wetland
11	Palustrine Emergent Wetland
12	Tidal Flats
13	Exposed Land (Bare Soil+Sand)
14	Water

Raytheon

Figure 17. Surface reflectance errors for 14 land surfaces (see Table 5) using MODTRAN3.7 forward and 6S backward. First column shows surface spectra, second column shows absolute errors, third column shows relative errors. Bands 1 through 6 correspond to first 6 bands in Table 3.

3.4.3   Aerosol Optical Thickness

Figure 18 and Figure 19 show the errors in surface reflectance encountered when the spec error for the Aerosol Optical Thickness EDR is applied to the input aerosol data, for the Bangladesh and Olympic Peninsula TERCAT scenes, respectively. In both cases, the shortwave bands are the most heavily impacted. This is to be expected, as aerosols have stronger scattering effects on short wavelengths. Bands in the shortwave infrared (SWIR) are affected to a much smaller degree.
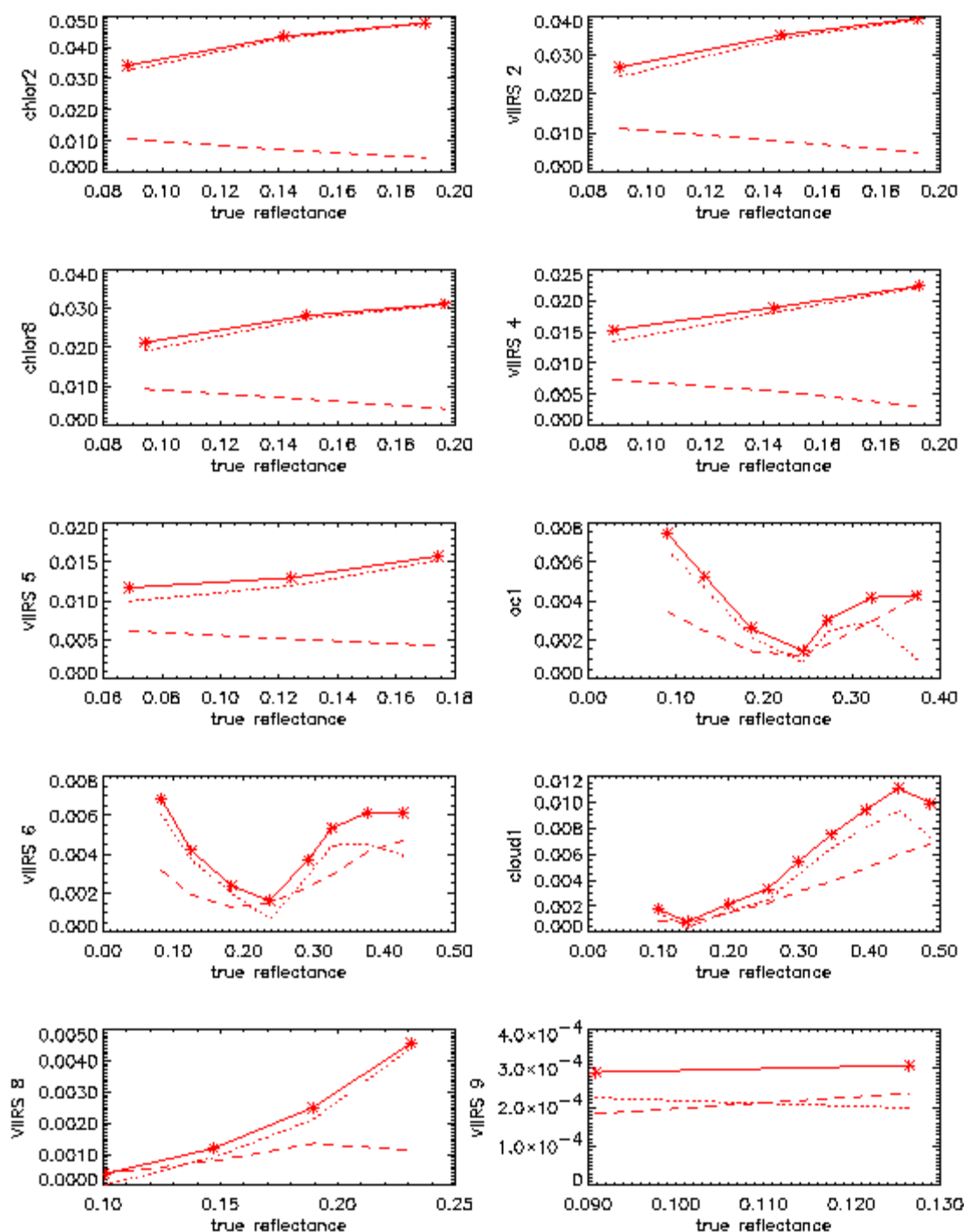
Figure 18. Accuracy (dotted), precision (dashed), and uncertainty (solid) in surface reflectance for 10 VIIRS bands due to spec errors in aerosol optical thickness, for the Bangladesh TERCAT scene.
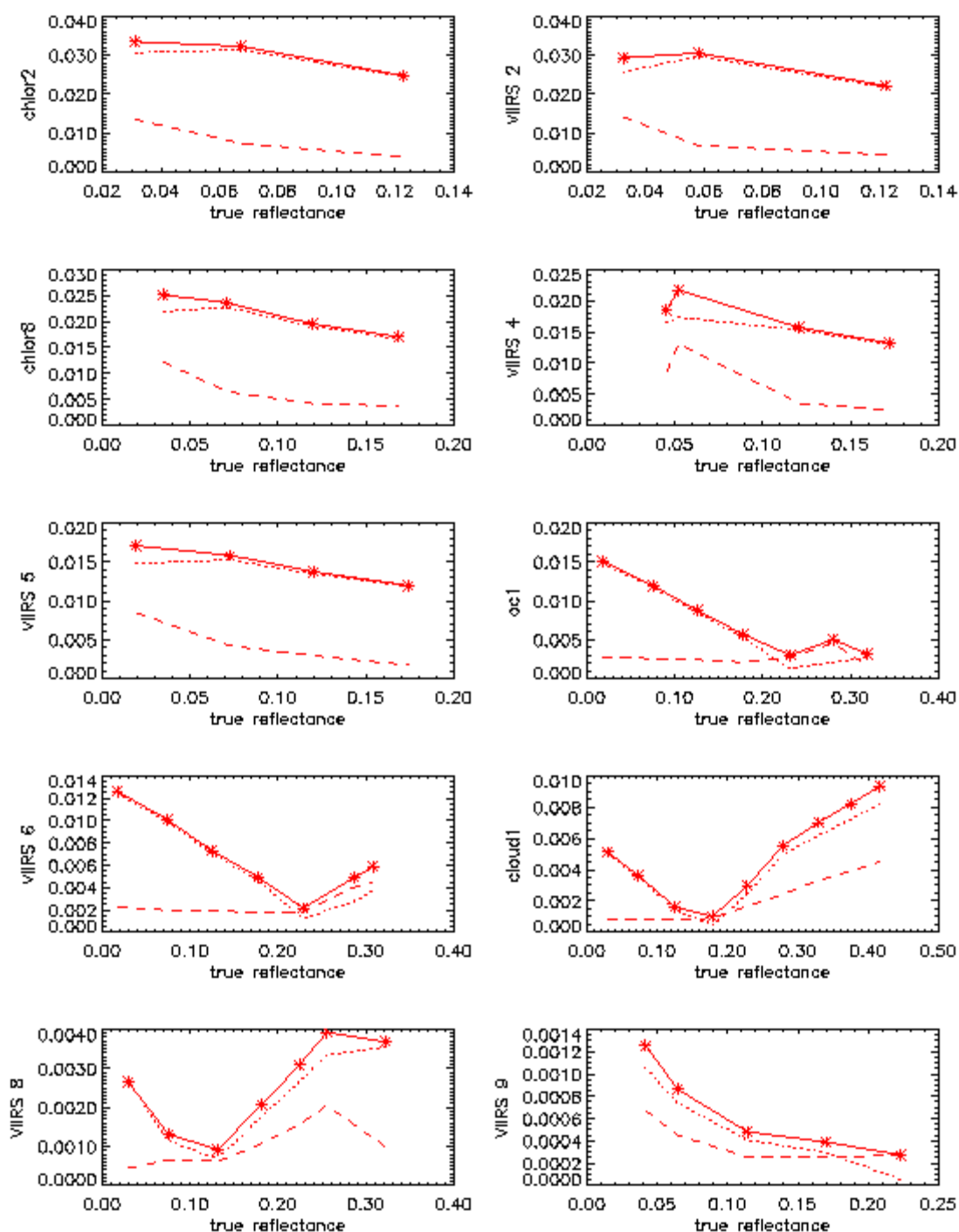
Figure 19. Accuracy (dotted), precision (dashed), and uncertainty (solid) in surface reflectance due to spec errors in aerosol optical thickness, for the Olympic Peninsula TERCAT scene.

3.4.4 Aerosol Type

Different aerosol models exhibit different phase functions and single scattering albedo, which can alter the effects of a single value of aerosol optical thickness from one type to another. Figure 20 shows the errors introduced by the misclassification of aerosol type before use of the surface reflectance LUT, with continental aerosols as the base type. The differences are noticeable for all misclassifications; the largest errors arise from the differences between the urban model (model #3) and other types available in 6S.

Aerosol type will be operationally reported along with Aerosol Optical Thickness for VIIRS, however this too will include some errors. Errors in aerosol type retrieval will be quite rare; the wealth of spectral information in the VIIRS bands, combined with the value of the optical thickness retrieval, will make misclassification an uncommon event. Additionally, when an error is made, it will be because two aerosol types are very similar, meaning their effects on TOA radiance will also be very similar, and therefore the error propagated into the surface reflectance LUT should be minimal. Since this is a small error occurring a small percentage of the time, it can be considered statistically negligible in the spirit of the SRD definitions of accuracy, precision, and uncertainty.
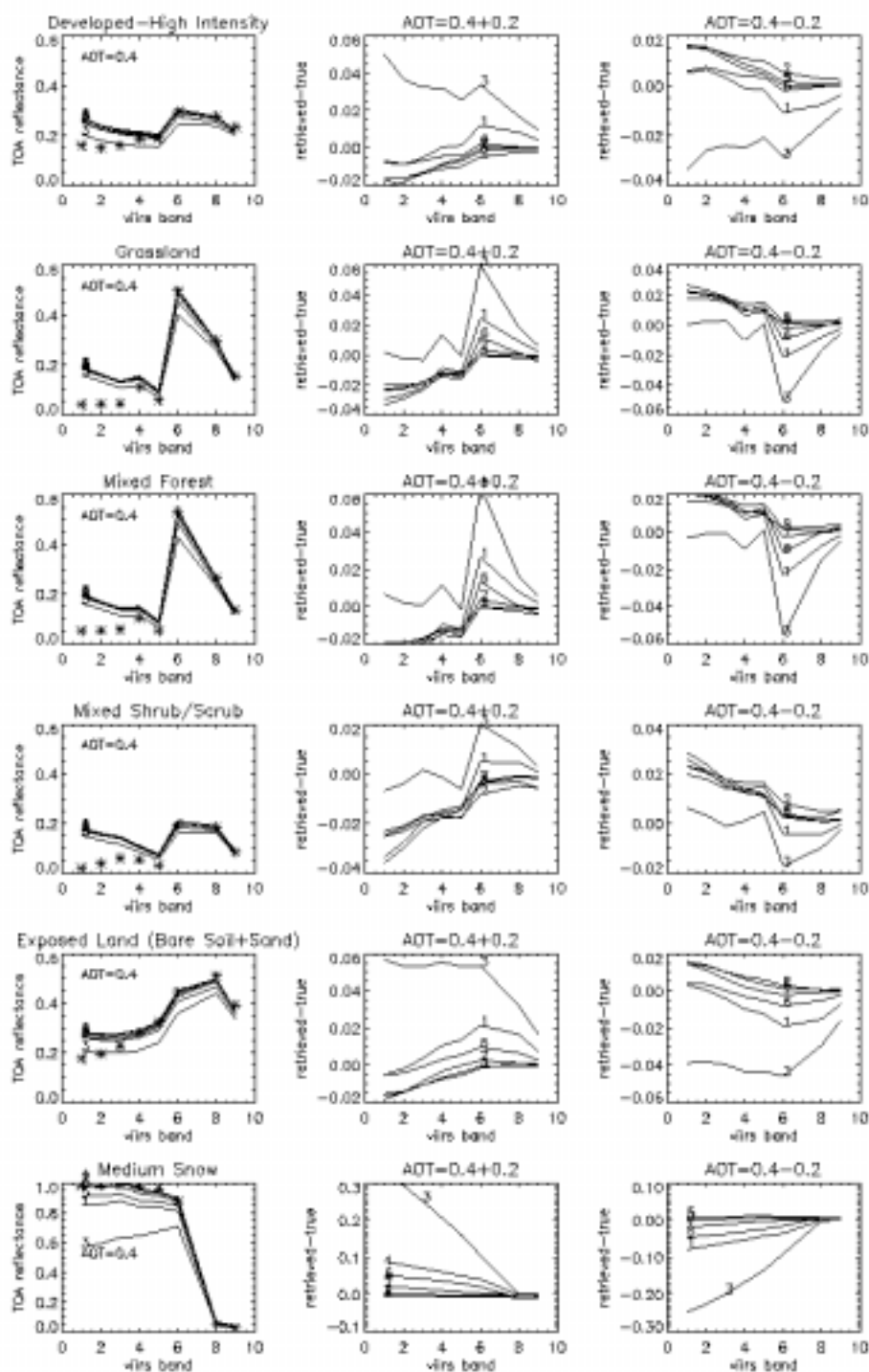
Figure 20. Differences in surface reflectance retrieval caused by misclassification of aerosol type. Column 1 shows TOA reflectance over different land surfaces using the continental aerosol model with AOT=0.4 (rather high). Column 2 shows the differences between retrieved and true surface reflectance resulting from the misclassification.

3.4.5 Column Ozone

Errors in the total column ozone lead to errors in retrieved surface reflectances. To investigate the magnitude of these errors, we ran 6S in a forward mode using the mid-latitude summer atmospheric model and the continental aerosol model with varying aerosol optical thickness. We then ran the backward mode of 6S with an error of ±15 Dobson units in the total column ozone (OMPS threshold) to retrieve the surface reflectances. In all cases, including snow, we found the errors in surface reflectance to be less than 0.003. Column ozone can therefore be considered a negligible source of error.

3.4.6 Precipitable Water Retrieval

Errors in the retrieval of precipitable water can also lead to errors in surface reflectance. In order to quantify this effect, the 6S model was run in a forward mode using the mid-latitude summer atmospheric model and the continental aerosol model with different aerosol optical thicknesses; then the backward mode of 6S was run with an input of 10 percent error in the total precipitable water column (CMIS threshold) to retrieve the surface reflectances. Again, the errors were consistently less than 0.003 in surface reflectance. Precipitable water can therefore be considered a negligible source of error. This and the results for column ozone should not be surprising; the VIIRS reflective bands were chosen in atmospheric windows to avoid absorption features.

3.4.7 Temperature Variations

To investigate the effects of different atmospheres, i.e., changes in the vertical profile of temperature, the 6S model in a forward mode was run using the mid-latitude summer atmospheric model and the continental aerosol model with different AOT. Then the backward mode of 6S was run with error of ± 1 K in the temperature profile to retrieve the surface reflectances. The results were perturbations of less than 0.001 in the surface reflectance for the shortest wavelength bands (blue and green), and virtually no error in the longer wavelength bands. Temperature is therefore considered a negligible error for surface reflectance.

3.4.8 Surface Pressure

Variations in atmospheric pressure, particularly near the Earth's surface, can have significant effects on the behavior of Rayleigh scattering through the vertical distribution of molecules. In order to analyze the uncertainty stemming from this effect, the 6S model was run in a forward mode using the mid-latitude summer atmospheric model and the continental aerosol model with different values of aerosol optical thickness. Then the backward mode of 6S was run with an error of pressure of ± 1 percent to retrieve the surface reflectances. The resulting errors were on the same order as those for gaseous absorption by ozone and water vapor, consistently below 0.003 reflectance units. Surface pressure is therefore considered a negligible source of error.

3.4.9 BRDF Coupling

The land surface reflects solar radiation anisotropically. This anisotropy leads to bowl-shaped distribution of surface reflectance in the solar principal plane, with a strong reflectance—the hotspot—where the solar and viewing directions are coincident. A bi-directional reflectance distribution function (BRDF) can been used to describe the anisotropy of the surface. For a

Lambertian surface, i.e., a surface that scatters light isotropically, radiative interactions between the atmosphere and its background can be built up rapidly in a geometric (doubling) manner, but an anisotropic land surface leads to a very complicated coupling between the atmosphere and the background surface. Failure to account for the surface BRDF effects in atmospheric correction can lead to significant errors in surface reflectance retrieval (Lee and Kaufman, 1986).

Several numerical radiative transfer models that make use of matrix operators, Gauss-Seidel, successive orders of scattering, and discrete ordinates methods have been developed for solving the coupling between the atmosphere and its lower boundary (Vermote *et al.,* 1997). Lyapustin (1998) uses spherical harmonics to model the coupling of the atmosphere and the non-Lambertian land surface. In this study, we employ the approach used in 6S, i.e., the Successive Orders of Scattering Method, to solve the radiative transfer equation in the atmosphere (Vermote *et al.,* 1997).

In the following, we analyze the effect of a non-Lambertian surface on the retrieval of bidirectional reflectance of land surfaces from VIIRS measurements. For a full study of this effect, we need to consider changes in solar zenith angle, aerosol optical thickness (AOT), the scattering phase function of aerosols, and different land surface types. As a preliminary study, the following only addresses the effect of a non-Lambertian surface on the TOA reflectance with different AOT over a conifer forest, and the retrieved error of the surface reflectance with a Lambertian-based atmospheric correction and a non-Lambertian-based atmospheric correction. Other factors will be addressed in future revisions of this document.

We ran the forward version of 6S for the coupling of surface BRDF and the atmosphere with different AOT values over conifer forests at different solar and viewing geometries. A hybrid geometric-optical and radiative transfer model developed for discontinuous plant canopies (Ni *et al.,* 1998) was used to generate the surface BRDF. The TOA bidirectional reflectances in the principal plane and across the principal plane with different AOT values for VIIRS bands 4, 5, and 6 (555 nm, 645 nm, and 865 nm, respectively) are shown in Figure 21 and Figure 22. The continental aerosol model and the mid-latitude summer atmosphere were used in the simulations. The surface BRDF values are also included in Figure 21 and Figure 22 for comparison. The figures show the following:

- The bidirectional reflectances in the solar principal plane (starred line as shown in the plots) show a bowl shape with a stronger hotspot at backward scattering. The atmospheric scattering makes this bowl shape much smoother than it would be without atmospheric scattering.

- In the principal plane, in the visible part of the spectrum (VIIRS bands 4 and 5), the TOA bidirectional reflectances overestimate the surface BRDF, due to more atmospheric Rayleigh scattering than absorption. This overestimation is larger with increased viewing zenith angles and even stronger in forward scattering than backward scattering due to the stronger forward scattering peak of aerosol particles. This effect increases in strength with the increase of solar and viewing zenith angles due to increased path length.

- In the near-infrared wavelengths (VIIRS band 6), the algorithm overestimates the surface reflectance in the forward scattering direction due to stronger forward scattering of aerosols and lower surface reflectances, leading to an atmospheric scattering effect that is a stronger than the absorption effect. Meanwhile, the algorithm underestimates the surface reflectances

in the backward scattering direction due to larger-surface reflectance and an atmospheric absorption effect that is stronger than the scattering effect.

- In the cross-principal plane, in VIIRS bands 4 and 5, atmospheric scattering causes an overestimation of the surface reflectances at solar zenith angles of 30° and 60°. In VIIRS band 6, at a solar zenith angle of 30 degrees, atmospheric scattering has virtually no effect on the surface reflectance, because atmospheric scattering and the absorption effect on the surface reflectance counterbalance each other. On the other hand, at a solar zenith angle of 60°, atmospheric scattering increases the surface scattering.

- A comparison of Figure 21 and Figure 22 shows that the atmospheric effect on surface reflectance intensifies with an increase of solar zenith angle due to the larger path lengths created.

We ran the Lambertian-based inverted version of 6S to retrieve the surface BRDF with the same atmospheric conditions as used in the forward TOA reflectance simulation. Figures 30 and 31 show the comparison of the retrieved and true bidirectional surface reflectances at solar zenith angles of 30 degrees and 60 degrees in the principal and cross-principal planes for VIIRS bands 4, 5, and 6. They show that:

- The retrieved bidirectional surface reflectances exhibit the bowl shape with a hotspot at backward scattering; in forward scattering the overestimations are not as strong.

- The correction does not fully correct the coupling of surface BRDF and the atmosphere. This correction is less desirable with increase of AOT.

- A comparison of Figure 23 and Figure 24 shows that this type of correction is less desirable with the increase of solar zenith angle.

The BRDF-based atmospheric correction was also run to retrieve the surface reflectance. The resulting comparison of the retrieved and true surface bidirectional reflectances is shown in Figure 25 and Figure 26. The results show significant improvements, but not perfection. The performance again degrades somewhat with the increase of AOT.
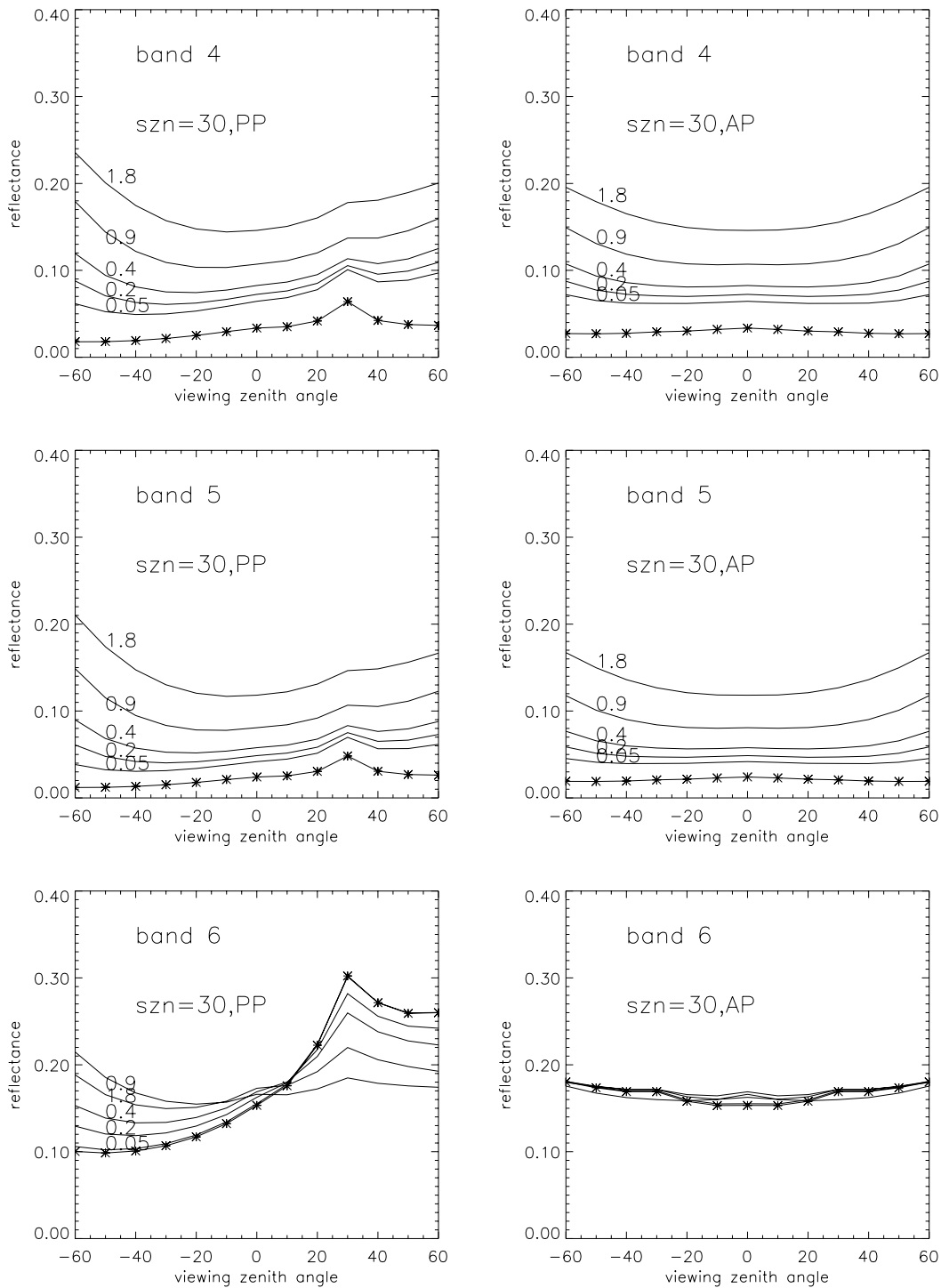
Figure 21. Comparison between surface (lines with *) and TOA (lines without *) bidirectional reflectance from 6S, in the principal plane (left) and the cross-principal plane (right) for VIIRS bands 4, 5, and 6 at 30 degree solar zenith angle with varying aerosol optical thickness. AP stands for "across principal plane;" PP stands for "principal plane."
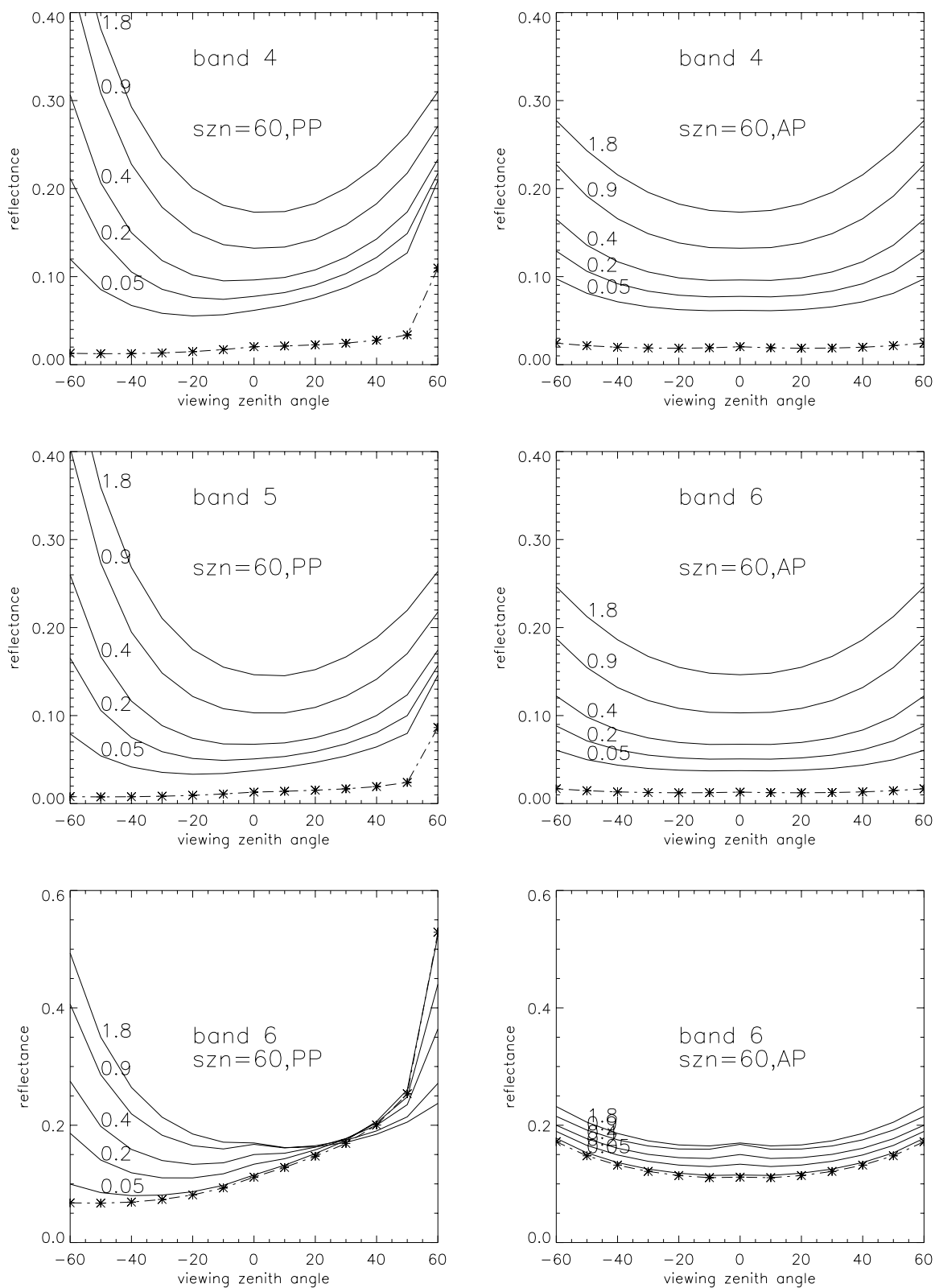
Raytheon

Figure 22. Same as Figure 21, except for a solar zenith angle of 60 degraerosol optical thickness. AP stands for "across principal plane;" PP stands for "principal plane."
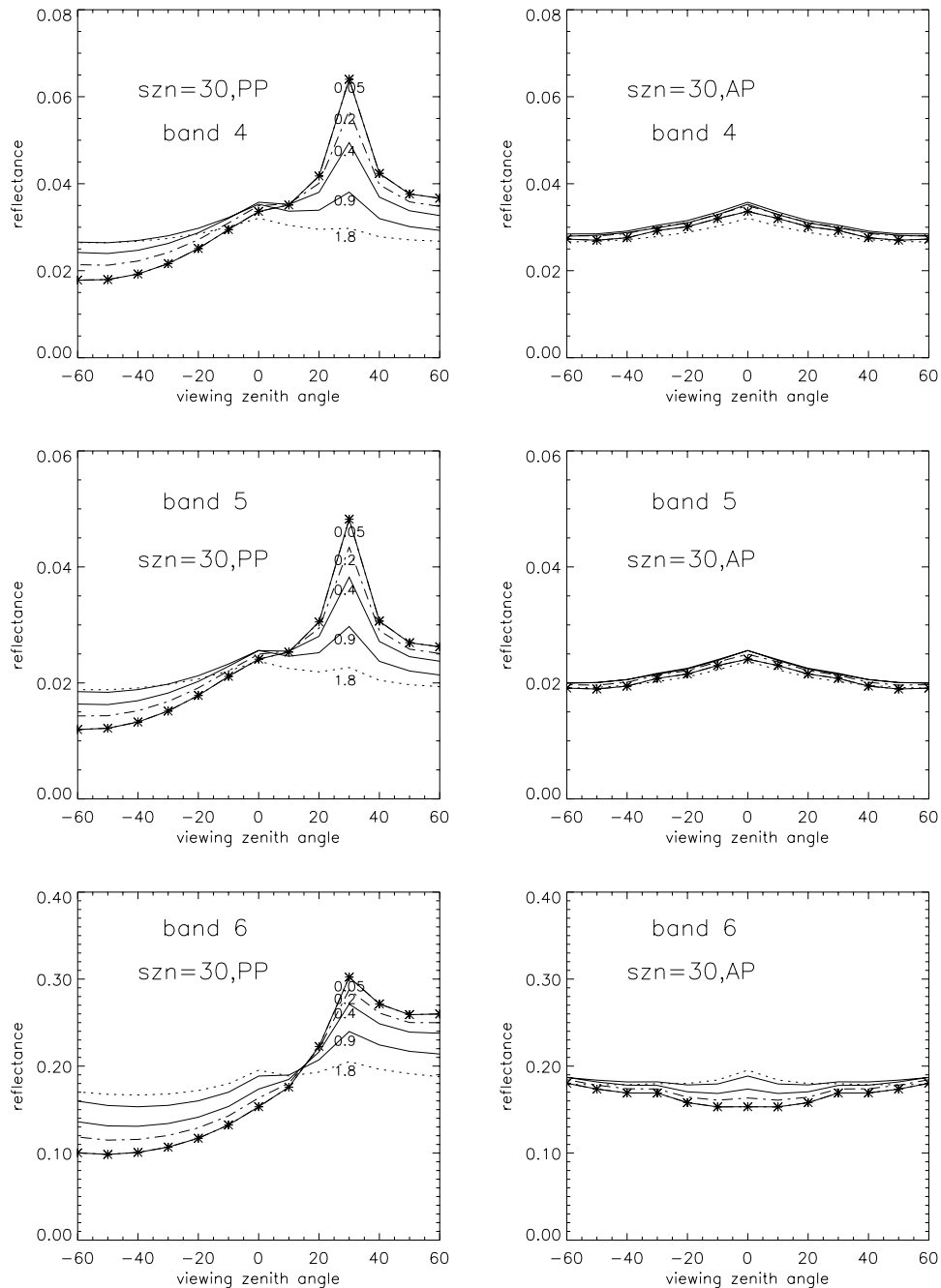
Figure 23. True (lines with *) and retrieved (lines without *) surface reflectances from 6S, using Lambertian-based atmospheric correction, in the principal (left) and cross-principal (right) planes, for VIIRS bands 4, 5, and 6 at a solar zenith of 30 degraerosol optical thickness. AP stands for "across principal plane;" PP stands for "principal plane."
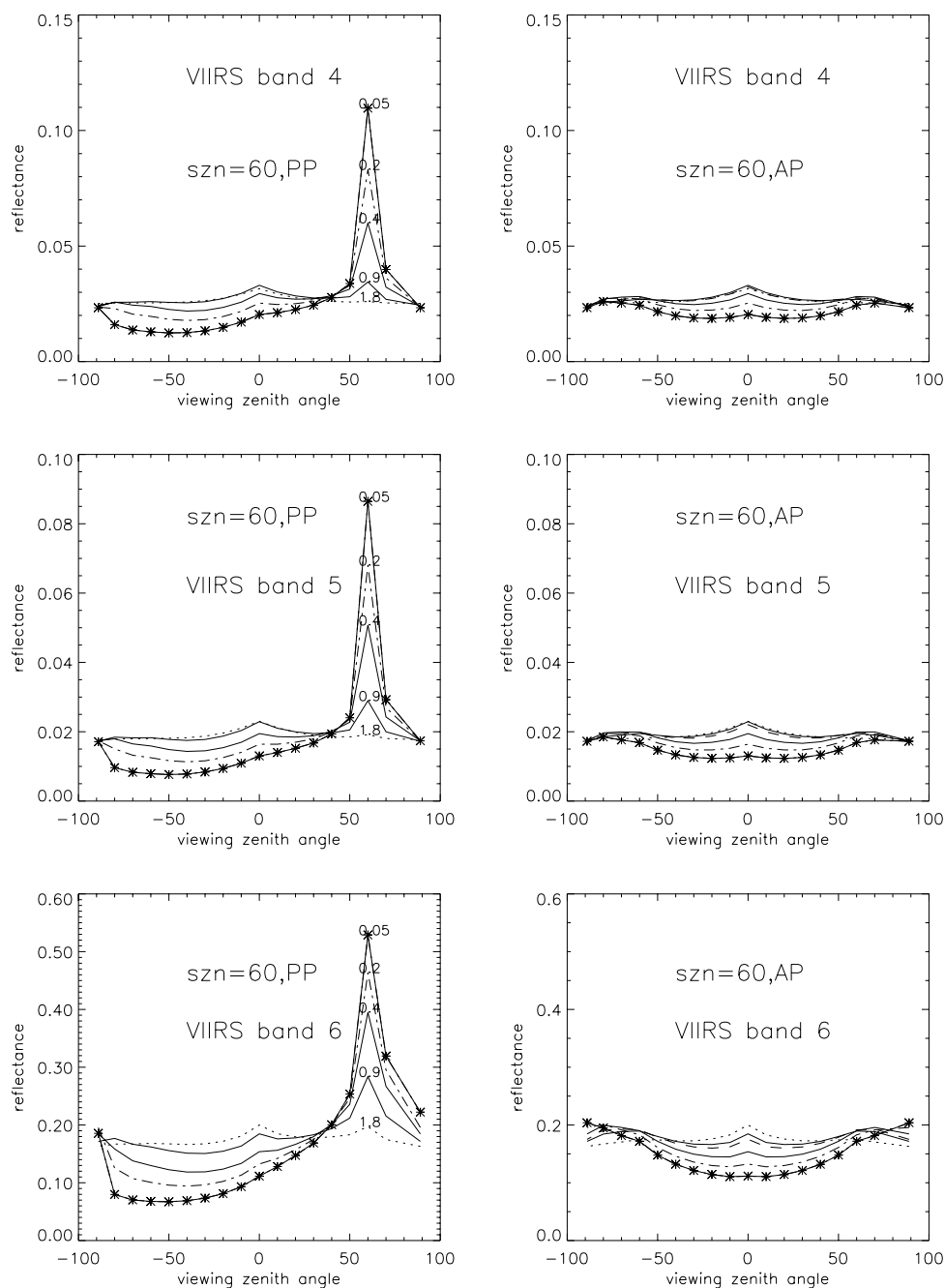
Figure 24. Same as Figure 23, for a solar zenith of 60 degraerosol optical thickness. AP stands for "across principal plane;" PP stands for "principal plane."
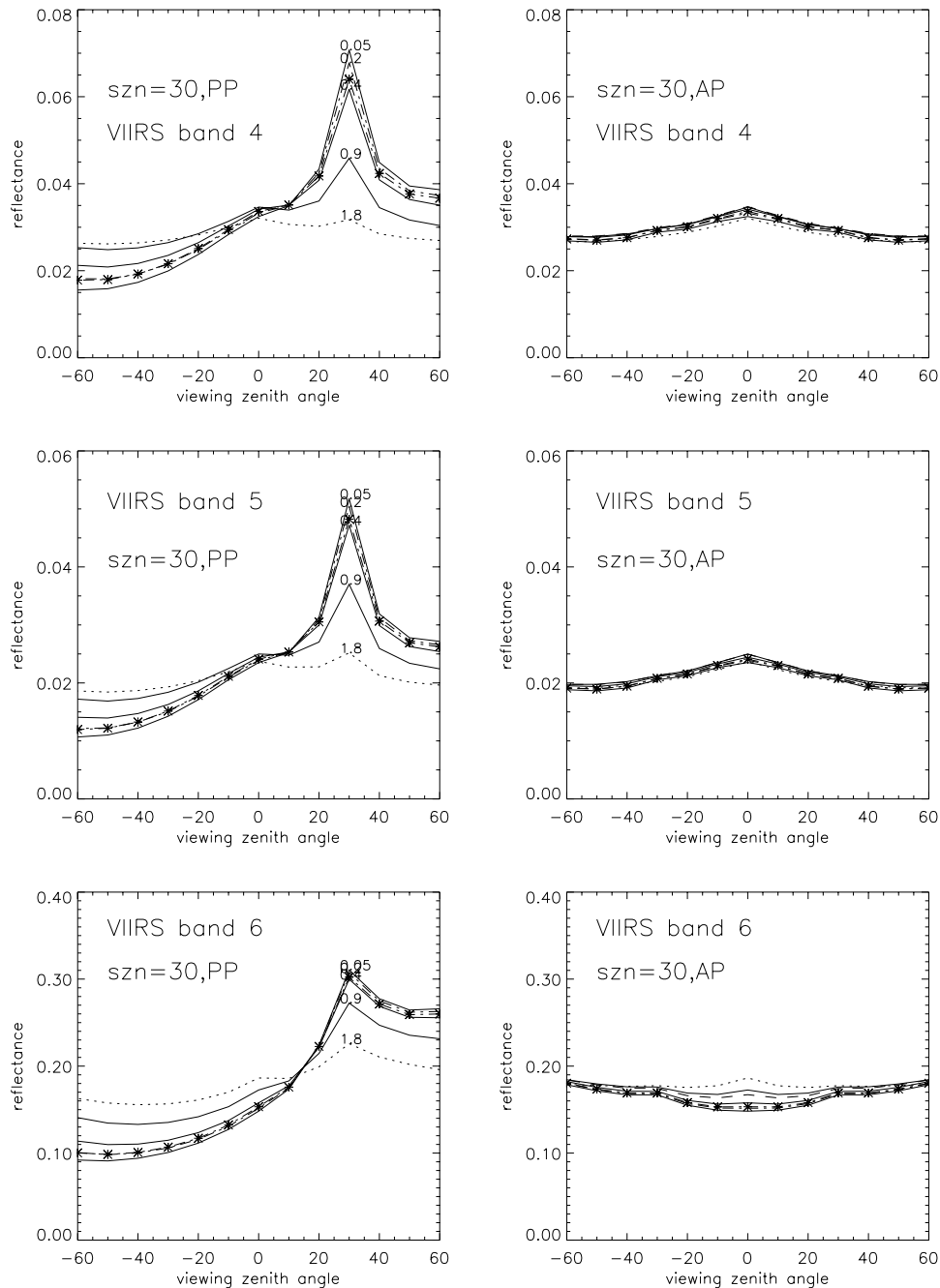
Figure 25. True (lines with *) and retrieved (lines without *) surface reflectances from 6S, using non-Lambertian-based atmospheric correction, in the principal (left) and cross-principal (right) planes, for VIIRS bands 4, 5, and 6 at a solar zenith of 30 degraerosol optical thickness. AP stands for "across principal plane;" PP stands for "principal plane."
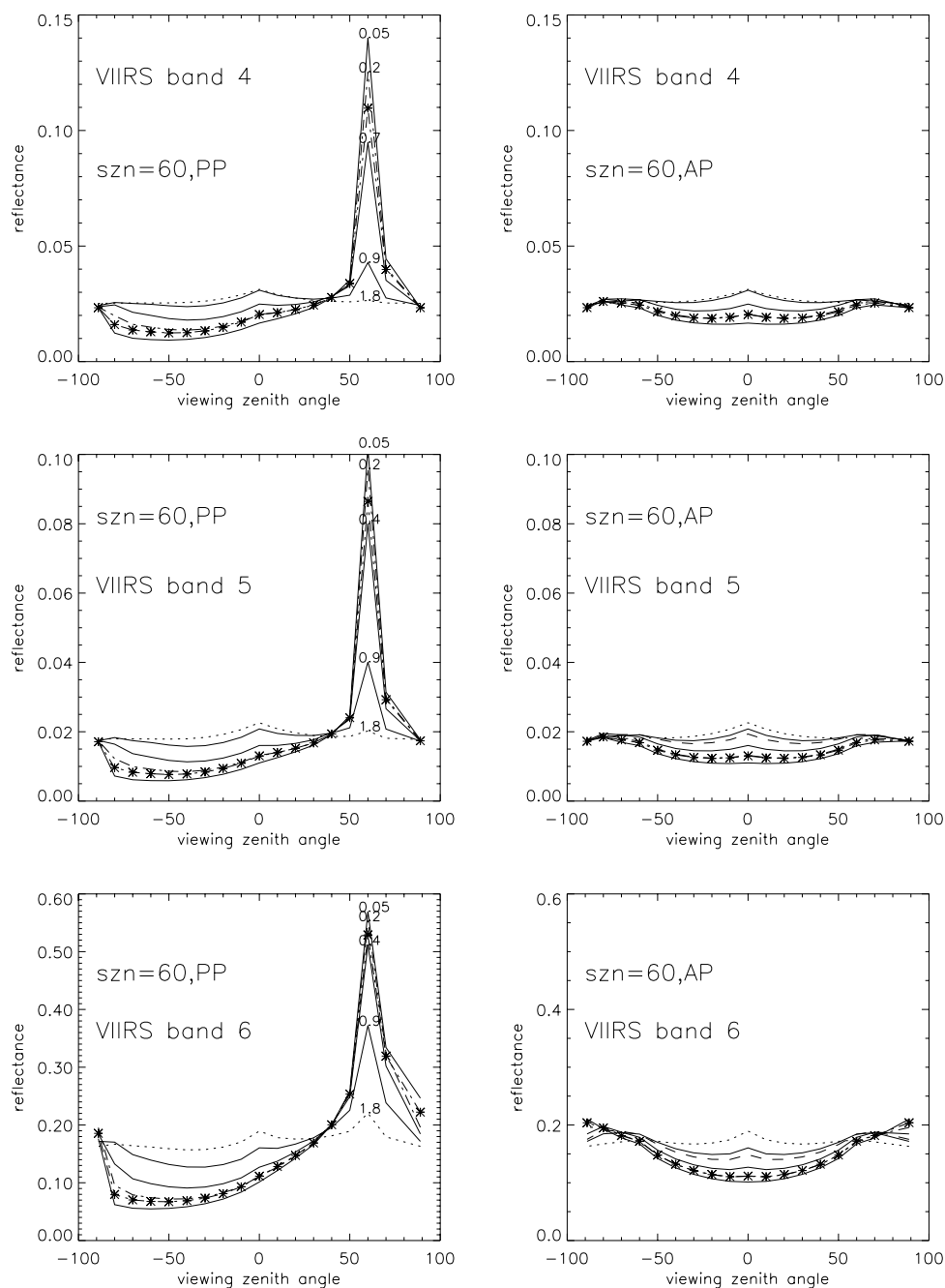
Figure 26. Same as Figure 25, for a solar zenith of 60 degraerosol optical thickness. AP stands for "across principal plane;" PP stands for "principal plane."

3.4.10 Cloud Mask Retrieval

The VIIRS software modules have not yet been comprehensively linked to allow a quantitative statistical determination of cloud mask errors in the spirit of the accuracy, precision, and uncertainty metrics as defined by the VIIRS SRD. The error is considered negligible, however, by the following reasoning.

The VIIRS Cloud Mask will screen out most cloudy pixels. Occasionally, however, the cloud mask will fail to detect a cloud, and in these instances the surface reflectance will incur an error. This error will tend to be small, because if it were not, the Cloud Mask would have flagged the cloud. Current performance appears to be on the order of 98% detection of clouds as clouds. This, combined with the small errors incurred for misclassification, leads to a conclusion that cloud mask error on a global statistical sense will be negligible compared to other error sources in surface reflectance retrievals.

3.4.11 Sensor Noise

Santa Barbara Remote Sensing (SBRS) constructed a simplified model of the VIIRS sensor that simulates various levels of noise for single pixel retrievals. This model is described in detail in Hucks (1998a). The model describes the sensor noise as a function of TOA radiance, L_{TOA} as,

$$\sigma = \sqrt{\alpha L_{TOA}} + \beta \tag{19}$$

where L_{TOA} is the TOA radiance, and σ is the standard deviation of the total sensor noise, assuming a Gaussian distribution. Although this assumption breaks down for very low radiances, it was deemed a sufficiently accurate approximation for simulations. α and β are two constants for a given level of sensor noise. We applied these constants as supplied by SBRS for a spec level of sensor noise in the appropriate bands, and for most bands the resulting errors were negligible, on the order of 0.005 reflectance units or less. The only band significantly affected by sensor noise is band 8i, an imagery-resolution band in a region of the spectrum where the solar signal is quite low. Aggregation of this band to moderate resolution, however, cuts the noise in half and renders the band sufficiently sensitive for use by the appropriate algorithms. For snow cover applications, aggregation is not necessary to provide the necessary level of performance.

3.4.12 Sensor Calibration

The spec level of 2% calibration error was applied to TOA radiances in our sensitivity studies to determine the magnitude of calibration effects on surface reflectance retrievals. The results for the Olympic Peninsula scene are shown in Figure 27.
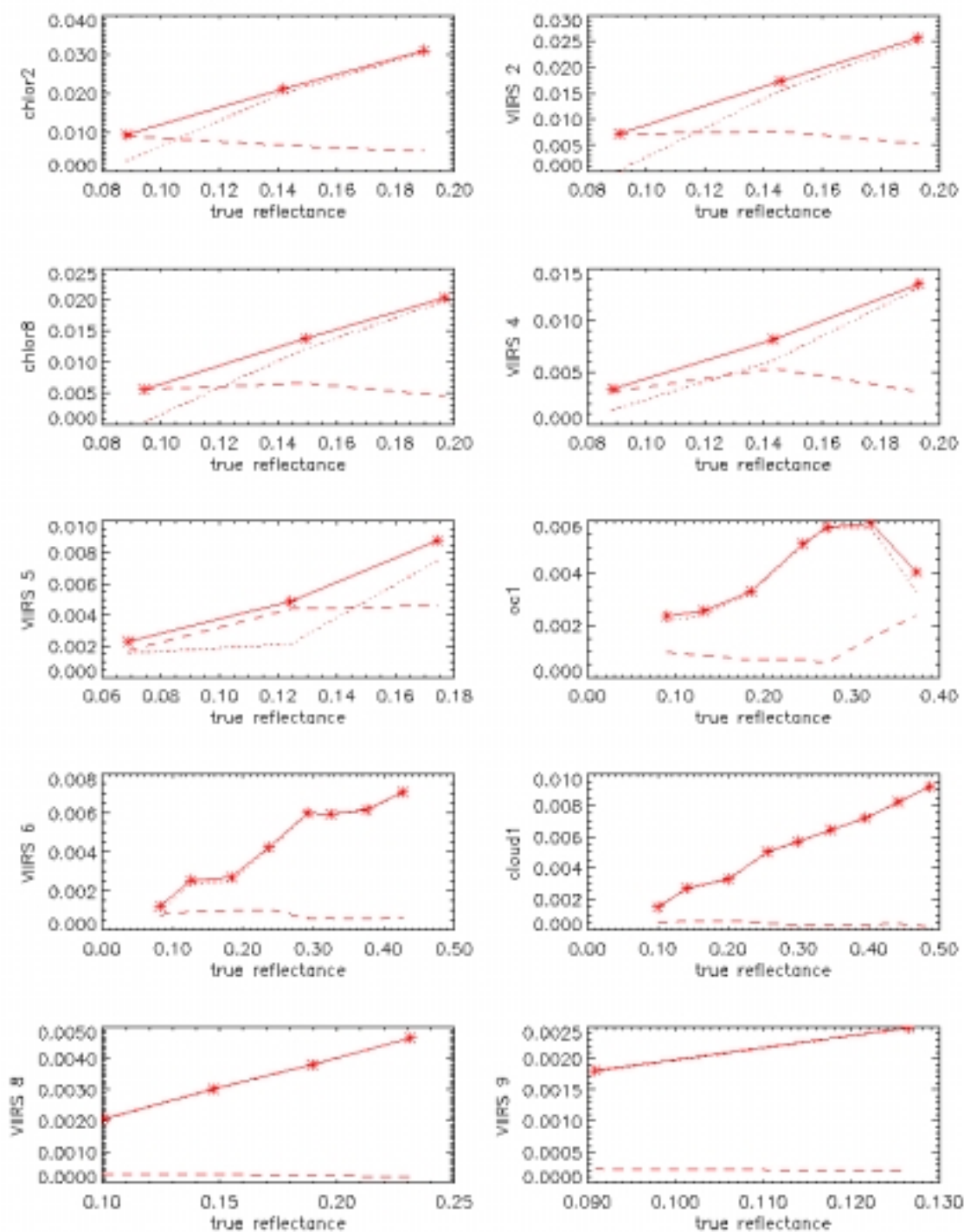
Figure 27. Accuracy (dotted), precision (dashed), and uncertainty (solid) in surface reflectance for ten VIIRS bands, due to calibration error of 2%.

3.4.13 Total Performance Stratification

To arrive at a total measure of performance for surface reflectance, stick models were generated as described at the beginning of Section 3.4. The results of the previous twelve sections were used to allocate errors due to temperature, pressure, ozone, water vapor, and forward modeling. Aerosol retrievals were simulated by adding the spec errors for the Aerosol Optical Thickness EDR to the true aerosol values. Calibration biases both up and down were considered, and the sensor specification and predicted performance for both noise and calibration were used to generate the results, which are summarized in Figures 28 through 36, for the nine VIIRS bands over which surface reflectance will be retrieved. The results are stratified by surface type, solar zenith, and viewing zenith (nadir versus edge of scan). These plots form the basis for the system specification for the Surface Reflectance IP.
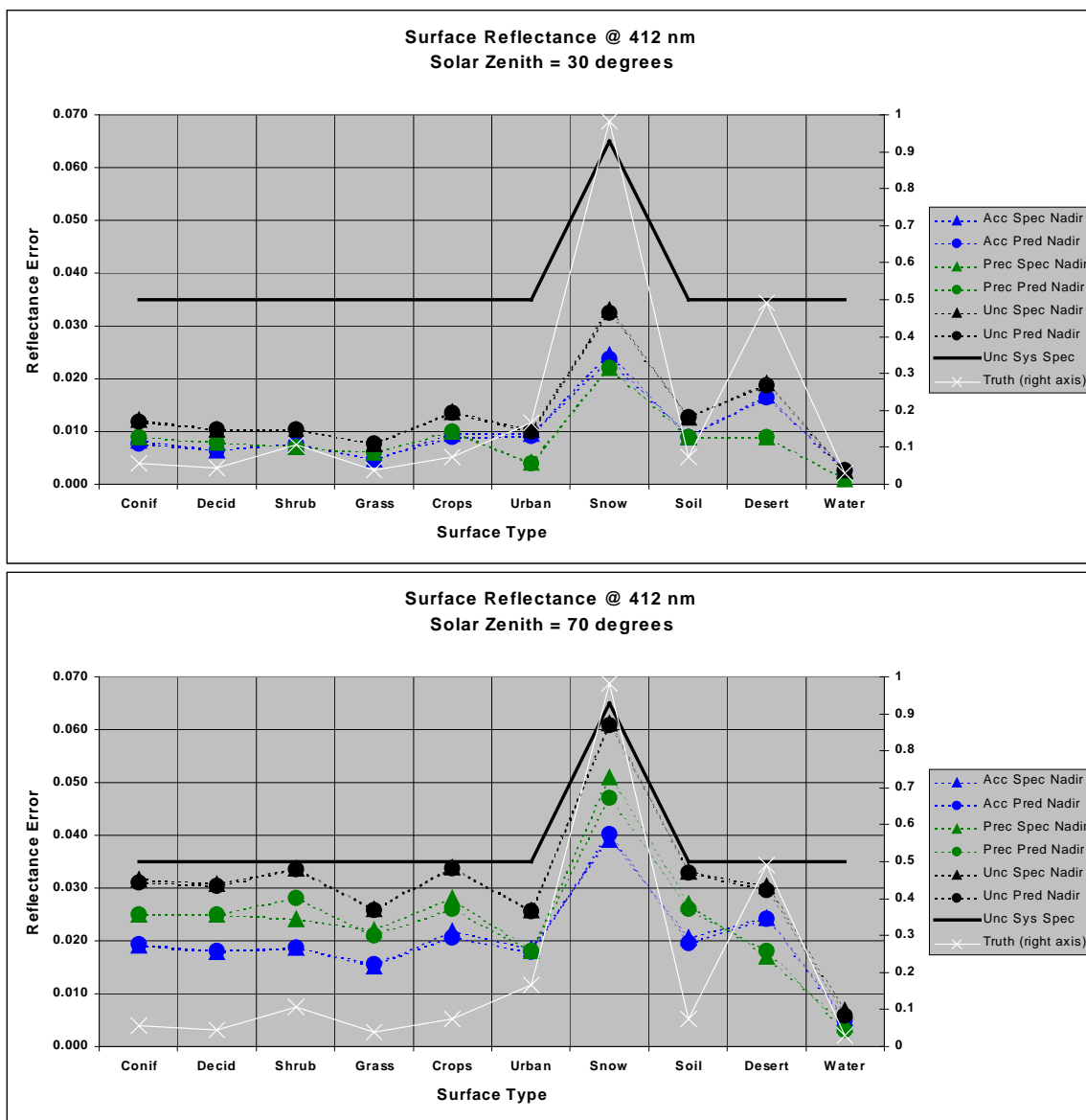
Figure 28. Stratified spec and predicted performance of the Surface Reflectance IP, at 412 nm.
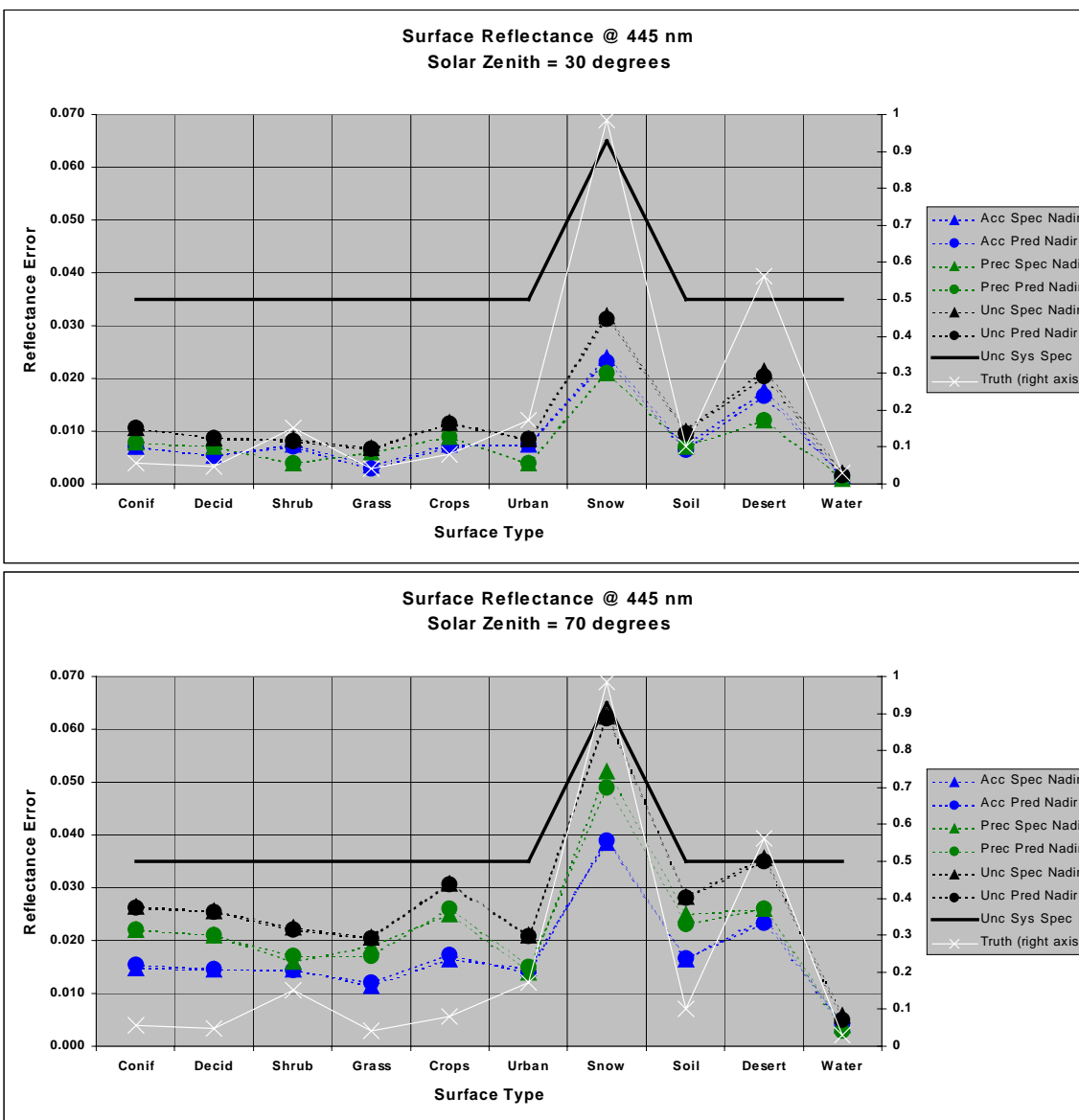
**Figure 29. Stratified spec and predicted performance
of the Surface Reflectance IP, at 445 nm.**

**Figure 30. Stratified spec and predicted performance
of the Surface Reflectance IP, at 488 nm.**

**Figure 31. Stratified spec and predicted performance
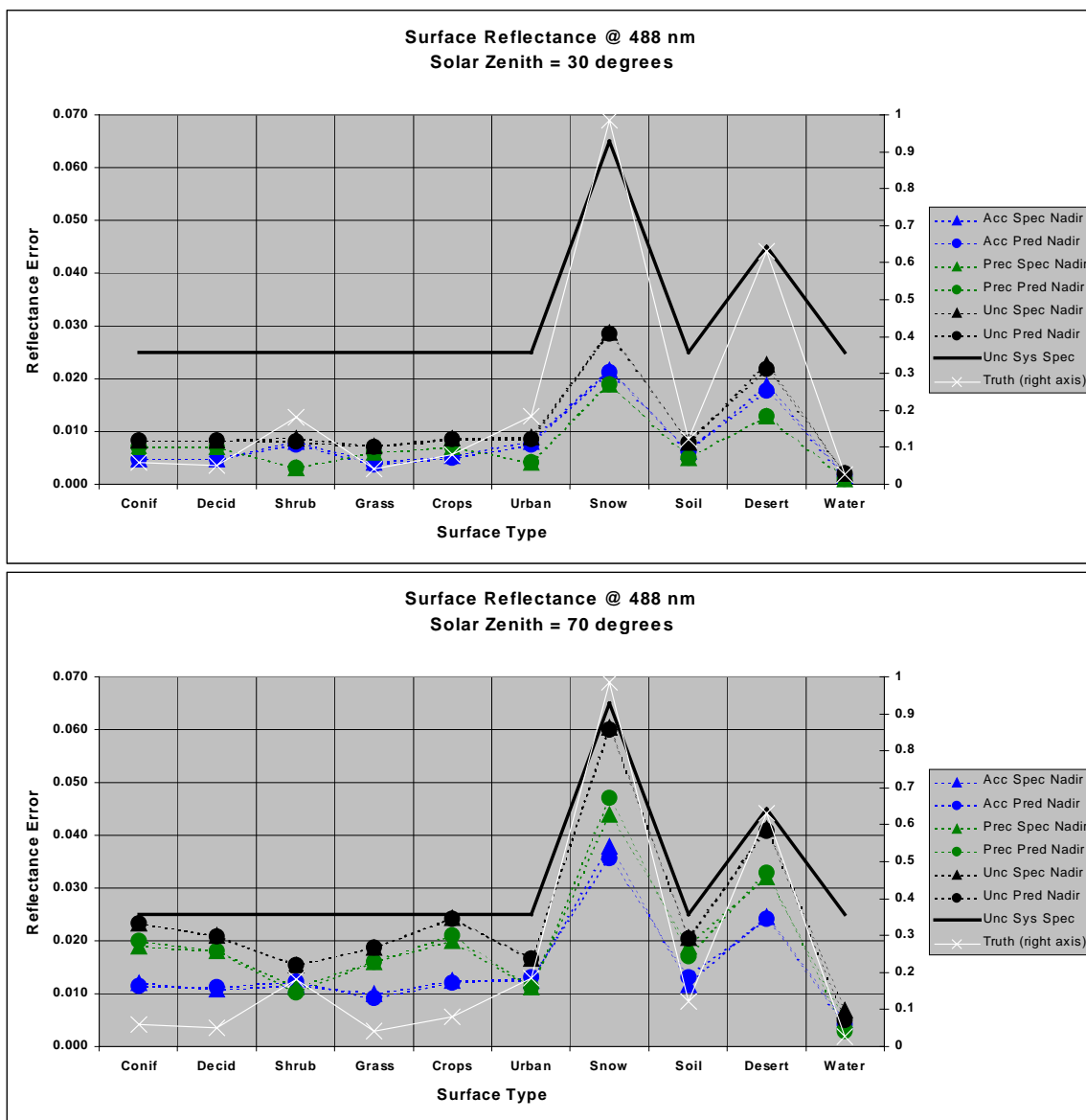of the Surface Reflectance IP, at 555 nm.**

**Figure 32. Stratified spec and predicted performance
of the Surface Reflectance IP, at 645 nm.**

**Figure 33. Stratified spec and predicted performance
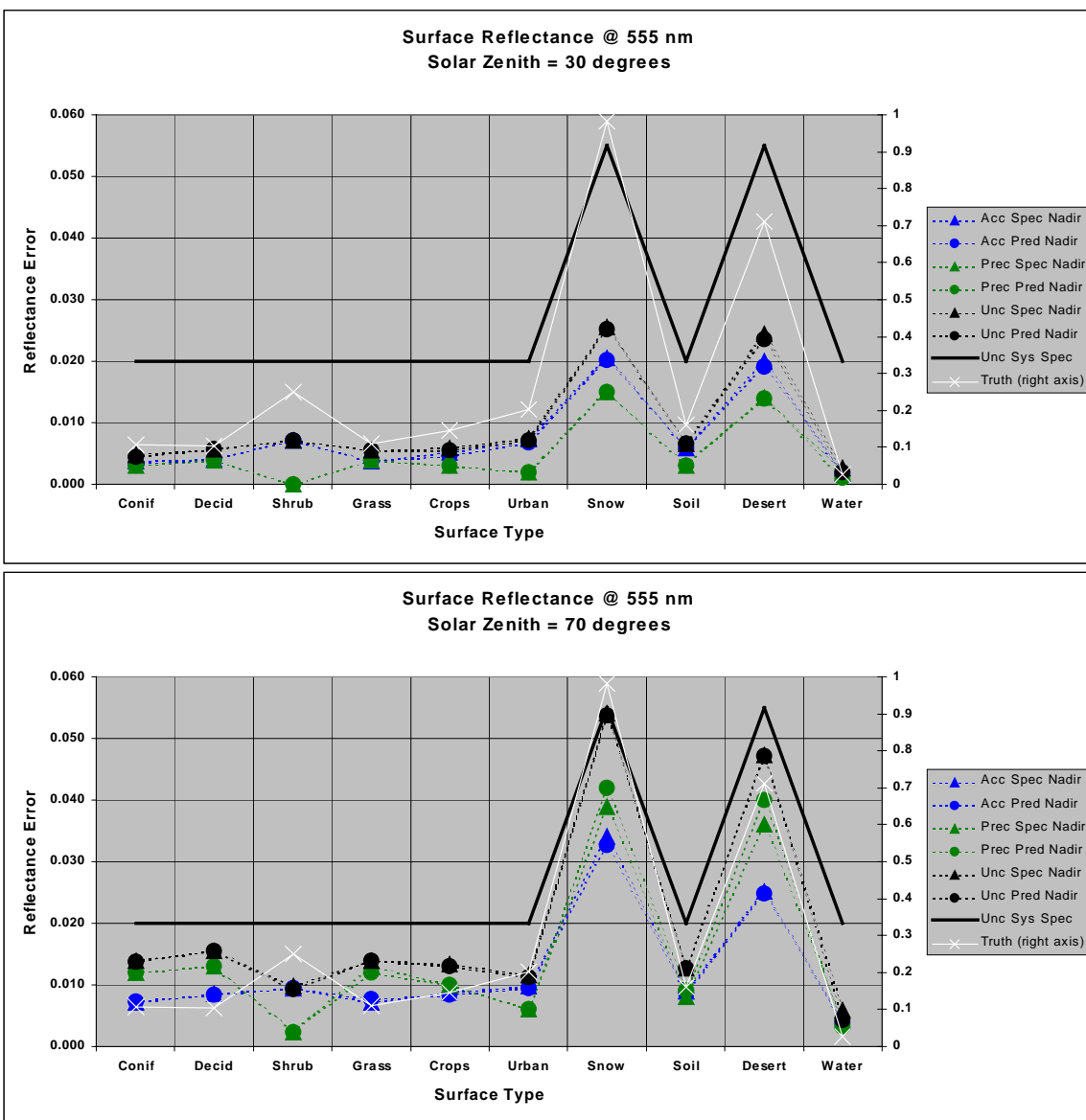of the Surface Reflectance IP, at 865 nm.**

**Figure 34. Stratified spec and predicted performance
of the Surface Reflectance IP, at 1240 nm.**
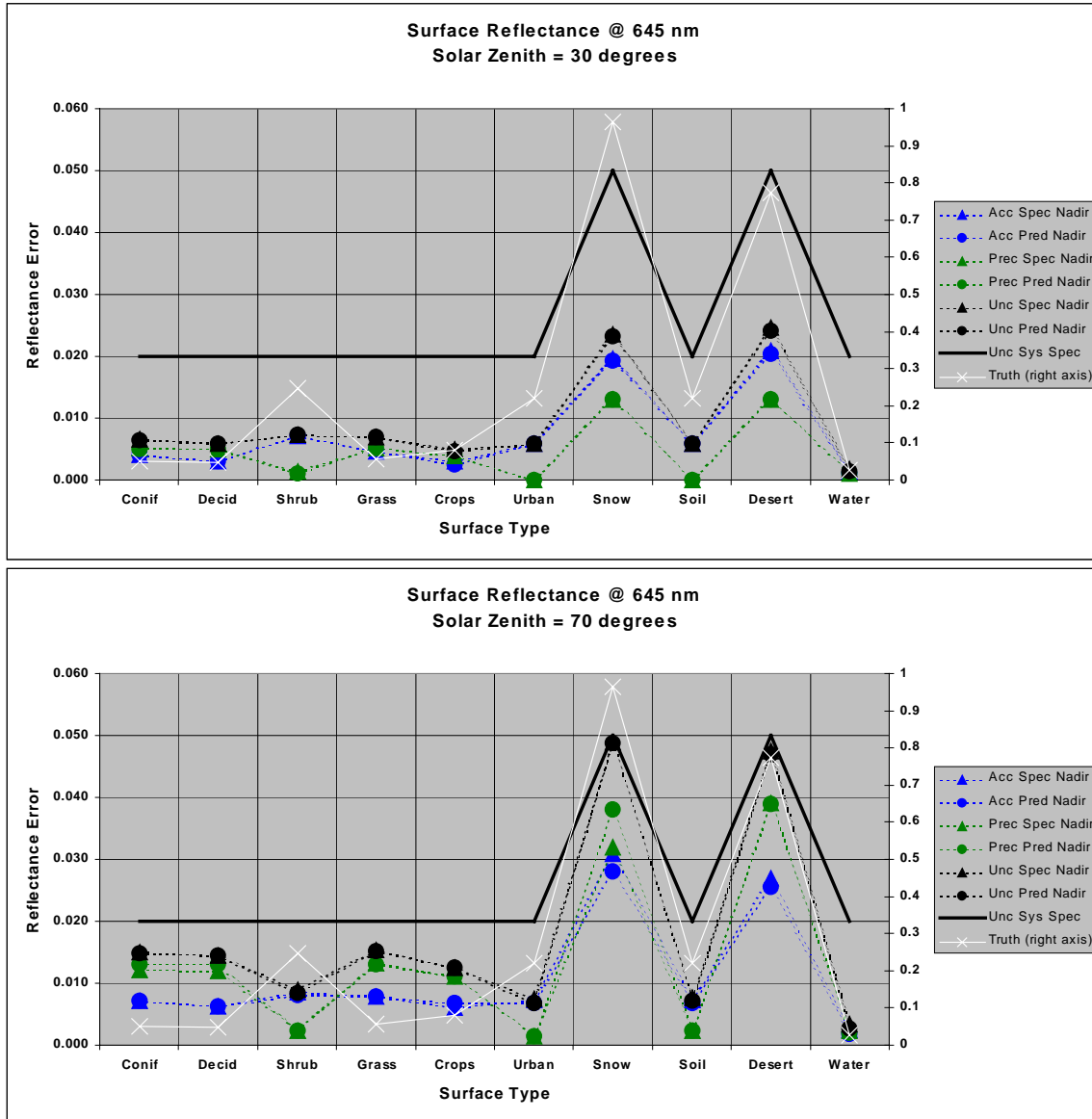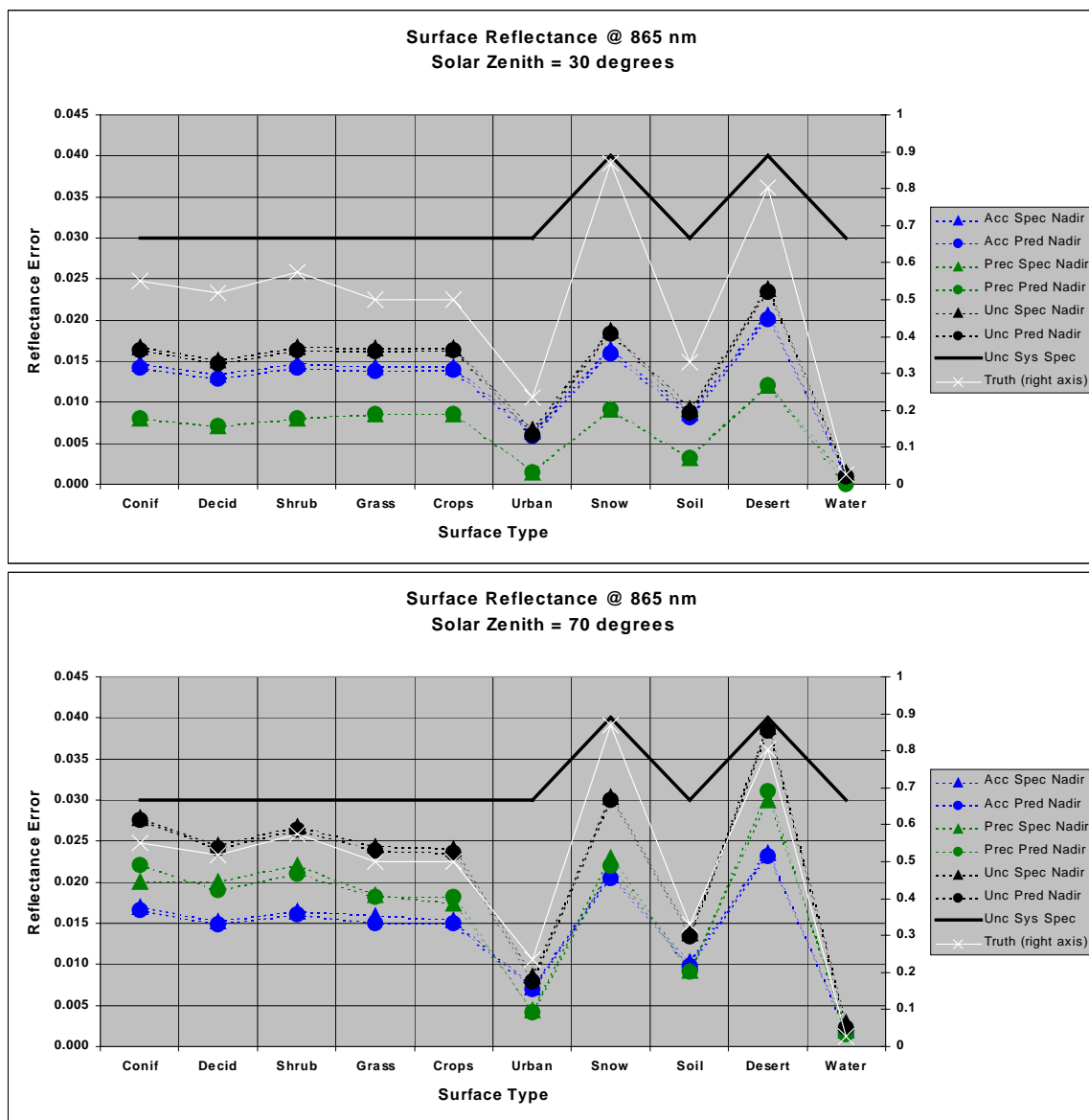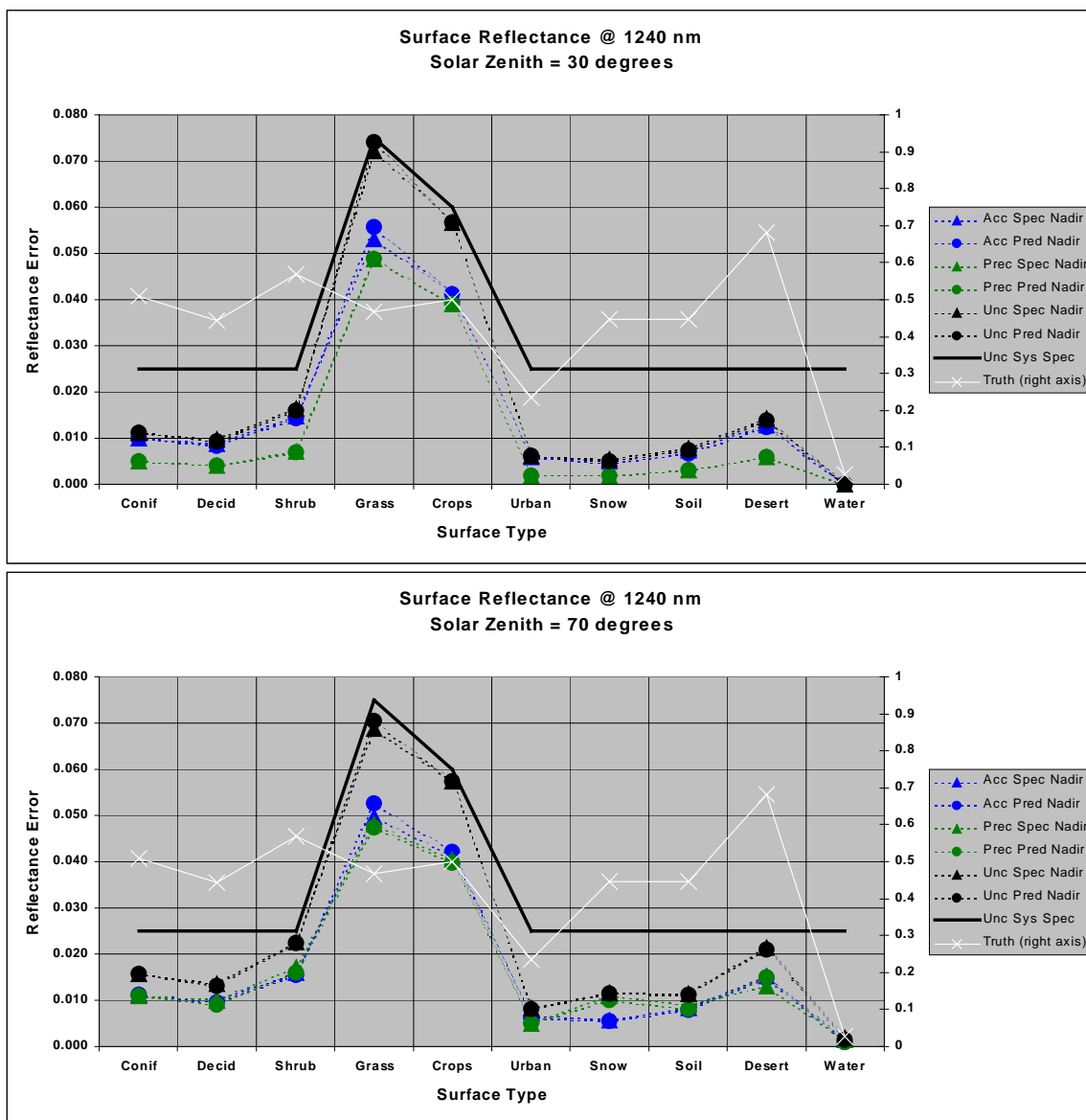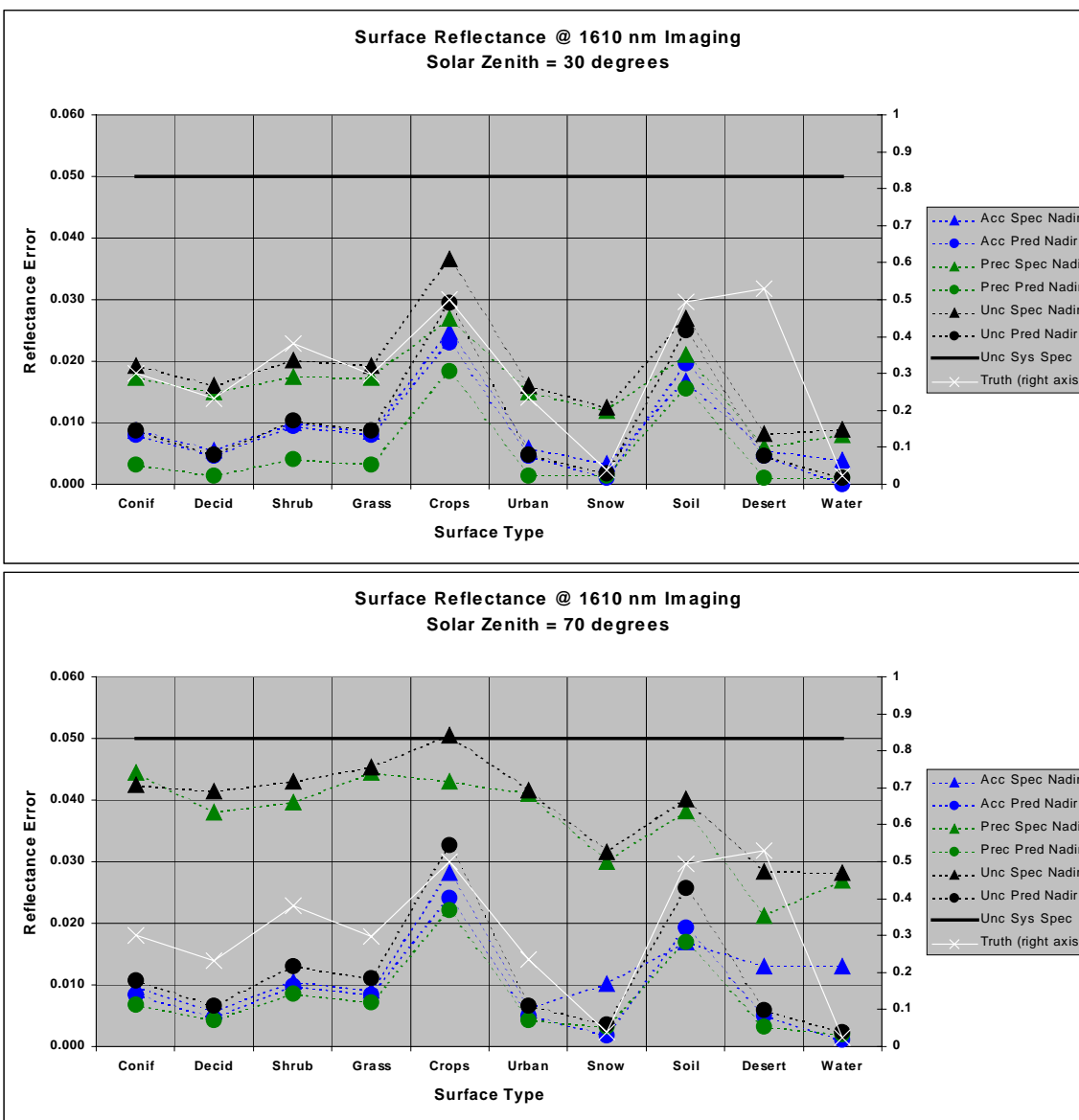
**Figure 35. Stratified spec and predicted performance
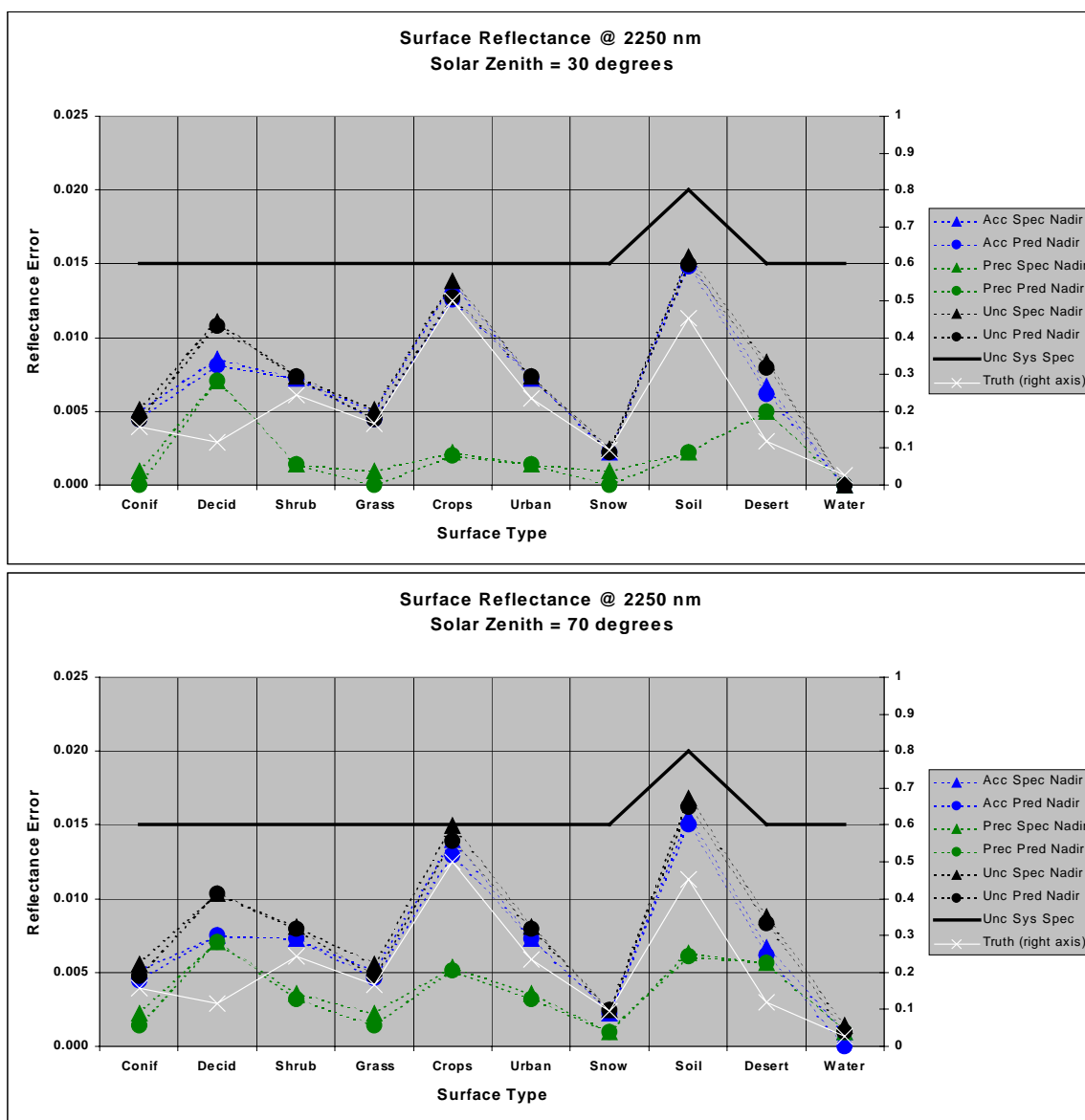of the Surface Reflectance IP, at 1610 nm.**

Figure 36. Stratified spec and predicted performance of the Surface Reflectance IP, at 2250 nm.

3.5   PRACTICAL CONSIDERATIONS

3.5.1   Numerical Computation Considerations

Paragraph SRDV3.2.1.5.4-1 of the VIIRS SRD states the following:

"The scientific SDR and EDR algorithms delivered by the VIIRS contractor shall be convertible into operational code that is compatible with a 20 minute maximum processing time at either the DoD Centrals or DoD field terminals for the conversion of all pertinent RDRs into all required EDRs for the site or terminal, including those based wholly or in part on data from other sensor suites."

RDR here stands for Raw Data Record. This essentially means that any and all EDRs must be completely processed from VIIRS raw data, including calibration and georeferencing within 20 minutes from the time a full orbit of raw data are available. This requirement is a strong reminder that VIIRS is an operational instrument.

For the Surface Reflectance IP, the challenges posed by the SRD time requirement are minimal. Application of the LUT will merely require the use of advanced programming techniques to minimize search time and I/O.

3.5.2   Programming and Procedural Considerations

Numerical computation load and complexity of operational code are typically rather well correlated. More intensive algorithms will generally be manifested in larger and more intricate source code. The code itself can have a significant impact on numerical computation load if it is not developed efficiently. The Surface Reflectance IP is not expected to cause many problems in this regard. The MODIS heritage will allow for the implementation of a low-risk, efficient LUT; the primary requirement will be for sufficient memory or storage to hold the LUT at processing time.

3.5.3   Configuration of Retrievals

The primary adjustable parameters for the retrieval of the Surface Reflectance IP are those which govern the overall stratification with respect to the expected quality of the output. These parameters are summarized in Table 6.

Table 6. Configuration of parameters for Surface Reflectance retrievals.

Symbol	Description	Current Value
θ_{0ques}	Solar zenith angle at which retrievals flagged as questionable	60°
θ_{0max}	Maximum allowable solar zenith angle	70°
f_{cques}	Threshold cloud fraction within HCS beyond which retrievals become flagged as questionable (probably clear will be processed along with definitely clear, but flagged)	0%
f_{cmax}	Maximum allowable cloud fraction within HCS	50%
AOT_{max}	Maximum allowable aerosol optical thickness	to be determined

Raytheon

3.5.4 Quality Assessment and Diagnostics

Operationally, quality control is automated for the Surface Reflectance IP, using the constraint parameters presented in Table 6. In order to ensure a high level of quality in the product, it is necessary to periodically perform manual inspections of both the input data and the processing scheme. The VIIRS team will use a variety of inputs to this process, including but not limited to surface-generated maps of vegetation cover, albedo, aerial photography and remote sensing of vegetation, data from other sensors, and statistical analyses.

The output of the Surface Reflectance IP is accompanied by the Land Quality Control Flag data, which include annotations concerning viewing/solar geometry, cloud cover, and general aerosol information.

3.5.5 Exception Handling

There are a number of situations encountered in practice that will preclude the accurate retrieval of the Surface Reflectance IP. In some instances, the degradation in accuracy is sufficiently small that the products are reported regardless. At other times, the degradation is high enough that retrieval becomes counterproductive. Table 7 summarizes the sources of exceptions for Surface Reflectance product generations, along with a brief description of the strategy for dealing with each source. If any of these sources is present as a significant contributor to the degradation in the product, the user will be notified via a corresponding flag in the quality control layer. The flags will be sufficiently categorized to clearly indicate the suspected source or sources of degradation for a given pixel.

Table 7. Exception sources and mitigation strategies for Surface Reflectance retrievals.

Exception Source	Strategy
AOT beyond AOTmax	Report, flag as obscured
Pixel flagged as probably cloudy or definitely cloudy	Don't report, flag as missing
Pixel flagged as probably clear	Report, flag as questionable
Solar zenith angle between θ_{0ques} and θ_{0max}	Report, flag as questionable
Solar zenith angle higher than θ_{0max}	Don't report, flag as nighttime
Geolocation unavailable or unreliable	Report, flag as unregistered

3.6 ALGORITHM VALIDATION

3.6.1 Introduction

Validation requires detailed knowledge of the relationship between measurables and geophysical quantities of interest over the full range of possible conditions. Pre-launch activities include determination of algorithms and characterization of uncertainties resulting from parameterizations and their algorithmic implementation. Post-launch activities include refinement of algorithms and uncertainty estimates based on near-direct comparisons with correlative data and selected, controlled analyses.

3.6.2   Pre-Launch Algorithm Test/Development Activities

The pre-launch validation will be performed by using MODIS data primarily, as the spectral bands are very similar and in many cases identical to those for VIIRS, and the algorithm is the same as well. The MODIS validation infrastructure, combined with international cooperative efforts such as LTER and GTER, will allow for rigorous validation without high cost or risk. Existing data sets have already played a role and will continue to do so; an example would be the AVHRR and Thematic Mapper (TM) data collected in the boreal ecosystem-atmosphere study (BOREAS) to retrieve surface reflectances. The atmospheric inputs can be obtained from *in situ* measurements made during the field campaign of BOREAS. For example, AOT can be obtained from sun-photometer observations made by AERONET; the atmospheric conditions will be obtained from other *in situ* measurements or climatological data sets. By comparing those retrieved surface reflectances with other multi-angular airborne measurements (POLDER, ASAS), PARABOLA measurements, and albedo measurements, we will address the accuracy, uncertainty, and precision of the retrieved surface reflectances at different cases, e.g., their dependencies on the angular sampling, surface conditions, and seasonal changes (for example, snow and no-snow background conditions).

4.0 ASSUMPTIONS AND LIMITATIONS

4.1 ASSUMPTIONS

This ATBD has included the following assumptions:

1. The applicability and validity of 6S and MODTRAN across the range of operationally defined solar zenith and viewing zenith limits

2. The availability of necessary non-VIIRS input data for operational retrievals

3. The availability of an aerosol climatology where aerosol retrievals cannot be performed directly over a large region

4.2 LIMITATIONS

Under conditions of extreme aerosol loading, such as that associated with biomass burning, local volcanic eruptions, or other similar events, performance is not guaranteed.

5.0 REFERENCES

Chandrasekhar, S. (1960). *Radiative Transfer*. New York: Dover.

Fraser, R. S., R. A. Ferrare, Y. J. Kaufman, B. L. Markham, and S. Mattoo (1992). Algorithm for atmospheric corrections of aircraft and satellite imagery. *Int. J. Remote Sensing*, 13(3), 541-557.

Holben, B., E. Vermote, Y. J. Kaufman, D. Tanré, and V. Kalb (1992). Aerosol retrieval over land from AVHRR data-application for atmospheric correction. *IEEE Transactions on Geoscience and Remote Sensing,* 30, 212-222.

Hucks, J. (1998). VIIRS Testbed sensor modeling efforts, Phase I. Raytheon Systems Company Internal Memorandum Y1629.

Lee, T. Y., and Y. J. Kaufman (1986). Non-Lambertian effects on remote sensing of surface reflectance and vegetation index. *IEEE Transactions on Geoscience and Remote Sensing,* GE-24, 699-708.

Leroy, M., J. L. Deuzé, F. M. Bréon, O. Hautecoeur, M. Herman, J. C. Buriez, D. Tanré, S. Bouffies, P. Chazette, and J. L. Roujean (1997). Retrieval of atmospheric properties and surface bidirectional reflectances over land from POLDER/ADEOS. *Journal of Geophysical Research,* 102(D14), 17,023-17,037.

Liang, S., H. Fallah-Adl, S. Kalluri, J. JáJá, Y. J. Kaufman, and J. R. G. Townshend (1997). An operational atmospheric correction algorithm for Landsat Thematic Mapper imagery over land. *Journal of Geophysical Research*, 102(D14), 17,173-17,186.

Lyapustin, A. I. (1998). Hemispheric surface albedo and BRDF. How are they related? Submitted to *Journal of Geophysical Research*.

Myneni, R. B., and G. Asrar (1994). Atmospheric effect and spectral vegetation indices. *Remote Sensing of Environment*, 47, 390-402.

Ni, W., X. Li, C. E. Woodcock, M. Caetano, and A. Strahler (1998). An analytical model of bidirectional reflectance over discontinuous plant canopies. *IEEE Transactions on Geoscience and Remote Sensing* (in press).

Tanré, D., B. Holben, and Y. J. Kaufman (1992). Atmospheric correction algorithm for NOAA–AVHRR products: Theory and application. *IEEE Transactions on Geoscience and Remote Sensing*, 30, 231-248.

Vermote, E. (1999). Spectral reflectances (MOD09). Version 3.0. Algorithm technical background document. *NASA EOS-1D 2015 Doc.*

Vermote, E. F., D. Tanré, J. L. Deuzé, M. Herman, and J-J Morcrette (1997). Second Simulation of the Satellite Signal in the Solar Spectrum, 6S: An Overview. *IEEE Transactions on Geoscience and Remote Sensing,* 35, 675-686.